



DTIC FILE COPY

A Surface Panel Method for the Hydrodynamic Analysis of Ducted Propellers

Justin E. Kerwin,¹ Associate Member, Spyros A. Kinnas,² Associate Member, Jin-Tae Lee,³ Student Member, Wei-Zen Shih,³ Student Member

The development of a panel method suitable for the analysis of ducted propellers is presented. The method is first applied to the problem of the two-dimensional hydrofoil, the propeller with hub and the axisymmetric duct in uniform flow. Some comparisons are made with exact solutions and with other panel codes. The difficulties associated with the modeling of ducted propeller flows are discussed. Convergence of the method for a typical ducted propeller is shown. The results include overall forces on the propeller and the duct, circulation distributions, and chordwise pressure distributions on the duct at different positions between blades.

DTIC
SELECTED
MAR 14 1988
C & E

1. Introduction

THE DESIGN of ducted propellers contains all the difficulties associated with the design of open propellers, including the conflicting considerations of efficiency, cavitation, strength, and vibration. However, one now has two complex geometries to deal with, thus increasing the number of variables in the problem, and increasing the complexity of the hydrodynamic problems which must be dealt with.

As with the case of open propellers, the approaches available to the designer vary greatly in complexity. One can simply select an existing geometry from published systematic series data, or one can develop a design which meets the unique requirements of a particular application. In the latter case, one must either trust in the accuracy of an existing analytical design method, conduct extensive model tests, or settle on some compromise between the two.

The disadvantage of model testing is that it is both time-consuming and expensive, thus limiting the extent to which a wide variety of design alternatives can be explored. This is certainly true for open propellers, but even more true for ducted propellers, where both the number of options to be studied and the complexity of the model test is much greater. Moreover, the ever-present question of scale effect errors is greater for ducted propeller tests due to the lower Reynolds number of the duct as compared to that of a rotating propeller blade.

A reliable analytical method for the hydrodynamic de-

sign and analysis of ducted propellers would therefore be desirable. This need has been recognized for many years, and substantial progress toward this goal has been made as a result of the contributions of a large number of researchers working in several distinct fields.

The largest element of previous research in ducted propellers has focused on the axisymmetric problem of a duct interacting with actuator disk, or equivalently, with an infinite-bladed lifting line. The earliest representations of the duct were fully linearized, with singularities representing the duct thickness and loading projected onto a mean cylindrical surface. This was extended to place the singularities on geometrically more complicated surfaces, to introduce some nonlinear aspects in the computation of pressures, and finally, to represent the duct more exactly by singularities placed on the actual duct surface. The work of Gibson and Lewis [1]⁴ and of Glover and Ryan [2] is representative of this stage of ducted propeller theory. More recently, Falcão de Campos [3] again retained an actuator disk model of the propeller, but introduced a numerical method to account for shear flow effects caused by a radially varying inflow field.

At the same time, propeller theory was advancing from lifting line theory to well-developed lifting-surface theories which could account for the increasingly complex geometries which were being adopted by propeller designers. Nevertheless, relatively few attempts to combine more exact representations of blades and ducts have appeared in the literature. Two recent publications which address this problem are by VanHouten [4] and Feng and Dong [5].

Another important source of research applicable to ducted propellers comes from the field of turbomachinery. In this case, of course, the flow is limited to the interior of a prescribed axisymmetric body where mass flow continuity immediately relates the upstream and downstream flows. Hence the similarity between the two problems is

¹ Professor of naval architecture, Department of Ocean Engineering, Massachusetts Institute of Technology, Cambridge, Massachusetts.

² Research engineer, Department of Ocean Engineering, Massachusetts Institute of Technology, Cambridge, Massachusetts.

³ Graduate students, Department of Ocean Engineering, Massachusetts Institute of Technology, Cambridge, Massachusetts.

For presentation at the Annual Meeting, New York, N.Y., November 11-14, 1987, of the SOCIETY OF NAVAL ARCHITECTS AND MARINE ENGINEERS.

⁴ Numbers in brackets designate References at end of paper.

RE: Distribution Statement

Approved for Public Release. Distribution Unlimited.

Per Professor Justin E. Kerwin, MIT, Dept. of Ocean Engineering

88 1 20 044

less when the duct is short relative to the propeller radius. On the other hand, the local flow between the propeller tip and the duct must be fundamentally very similar. Samples of the extensive literature in this field are papers by Lakshminarayana [6] and by Booth, Dodge and Hepworth [7].

The development of methods for treating axisymmetric shear flows is also an important aspect of turbomachinery theory, and much of this is applicable to the ducted propeller problem. An example is the streamline curvature method presented by McBride [8].

Finally, the broad field of discretized boundary integral methods has application to the specific problem of the ducted propeller.

In this paper we concentrate on the formulation and numerical solution of the steady, potential flow problem of a duct, hub and propeller with a finite number of blades. Except for the tip flow problem, which we address briefly, real fluid effects will not be considered. Our objective is to develop a robust potential flow foundation for the flow produced by geometrically complex ducted propellers.

2. General discussion of panel methods

Discretized boundary integral methods, more commonly referred to as *panel methods*, are rapidly becoming an essential tool for the analysis of flows around complex three dimensional objects. Since the publication of the pioneering work of Hess and Smith [9] in 1964, a large number of different panel methods have appeared. Some of these can be categorized as production codes, which can be used for a wide variety of applications. Surveys of some of the major production codes may be found in publications by Hess [10], Hunt [11], Margason, et al [12], Maskew [13], and Youngren et al [14]. Others are special purpose codes which have been developed with specific applications in mind. Examples of the latter are the propeller duct code developed by Gibson and Lewis [1] which we discussed earlier, and a recently developed propeller panel code presented by Hess and Valarezo [15].

The governing equation for most of the original panel methods was the requirement that the normal velocity be zero at a selected point on each panel. Subsequently, Morino [16] introduced a panel method based on Green's formula in which the primary unknown was the potential. Both velocity and potential methods are in current use, and each has its advantages and disadvantages.

In addition to this fundamental difference, various combinations of source, vortex and dipole singularities are employed in the various methods. This might seem arbitrary, since there is only one unique solution for a given body geometry and inflow field. The explanation is that different formulations yield different flows internal to the body, but identical flows in the exterior field. Since the internal flow has no physical significance, different distributions of singularities on the boundaries of a body can produce same correct physical flow. A brief but rigorous derivation of the equivalence of velocity and potential formulations, and of the relationship between the types of boundary singularities is presented in Appendix 1. This can be summarized with the happy conclusion that everybody is right!

A numerical implementation of any of these fundamental approaches involves approximations of various sorts, and it is here that various methods differ. The body surface can be approximated by plane quadrilateral elements with constant singularity density within each panel, or by curved panels with varying singularity densities. Methods

employing the former are termed *low order panel methods* while the latter are referred to as *high order methods*. High order methods can achieve a prescribed level of accuracy with fewer panels, but the code is more complicated and the required amount of computation per panel is higher. Since the relative merits of low and high order methods depend both on the specific problem and on the fundamental method being used, it is not surprising that the issue is controversial.

Finally, problems involving lift require the imposition of a Kutta condition at the trailing edge. Implementation of the Kutta condition in a discretized problem again involves approximations, and these vary between methods.

A comprehensive study of the field of panel methods has recently been conducted by J.-T. Lee [17] in order to determine the most suitable formulation for application to marine propeller and duct problems. The conclusion was that a low order potential based panel method, coupled with nonlinear pressure Kutta condition, would be best. Some of the principal reasons for this conclusion are,

- While practically all methods work well for thick sections, the potential method is substantially more accurate for very thin sections. This is particularly important for marine propellers, where thickness/chord ratios typically vary from 20 percent at the root to as little as 2 percent near the tip.
 - The influence coefficients for a potential induced by unit source and dipole distributions are one order less singular than the corresponding influence coefficients for velocity. As a result, potential based methods are expected to be less sensitive to errors caused by irregular paneling.
 - The computation of the panel influence functions, which is a major contributor to the total computing effort, is faster for a potential method than for a velocity method. Of course, one must eventually determine velocities in order to obtain the pressure distribution. However, this can be accomplished in a more accurate and efficient way by differentiating the potential than by direct computation of the velocities induced by the panel singularities.
 - Since the potential influence coefficients are scalar quantities, the total storage required is one third as great as for a velocity method.
 - A low order potential method is substantially more accurate than a low order velocity method for the computation of internal flows. This problem is, of course, of direct concern in the ducted propeller problem.
 - A low order potential method is probably computationally more efficient than a high order velocity or potential method for incompressible flows. Even if this were to be proved subsequently not to be the case, we would never know unless we had an efficient low order code to serve as a basis for comparison.
- A panel calculation for the flow around a body with lift involves the following relatively independent steps,
- grid generation,
 - development of logic to take advantage of symmetry,
 - computation of the panel singularity influence functions,
 - solution of the simultaneous equations for the unknown singularity strengths,
 - determination of local velocities and pressures, and
 - determination of total forces and moments.

While the major emphasis in this paper is on the ducted propeller problem, this represents systematic evolution of

the application of panel methods to two-dimensional hydrofoils, propellers with hubs, isolated ducts and, finally, propellers with hubs and ducts. We will therefore describe how each of these steps is accomplished as the present method is applied to all four of these problems. While we will not be discussing the structure of the computer codes, it is important to note that all of these problems contain common elements which can be individually programmed and combined in a way which is most efficient for the problem at hand.

3. The two-dimensional hydrofoil

The essential first step in a panel procedure is the generation of accurate coordinates for the vertices of each of the panels representing the body. Any unfairness introduced by an imperfect interpolation process will result in a bumpy pressure distribution. Most hydrofoil sections are defined by the superposition of a mean line and a thickness form, and as long as both are defined analytically, or are approximated by cubic splines passing through an accurate set of base points, the required degree of smoothness is easy to achieve. Sections generated by conformal mapping are frequently useful to compare numerical and exact solutions. In this case, the evaluation of the section at the desired grid points can be carried out to any desired degree of precision.

The next step is to devise a systematic way of determining the spacing of the panels, given their total number. For a two-dimensional hydrofoil, an arrangement commonly referred to as *cosine spacing* is a logical choice. For a given total number of panels, N , the mean line ordinate and thickness is first evaluated at the following points along the nose-tail line,

$$x_j = \frac{c}{2} \left(1 - \cos \left(\frac{2\pi(j-1)}{N} \right) \right),$$

$$j = 1, 2, \dots, N/2 + 1 \quad (1)$$

where x is the coordinate along the nose-tail line of a section of chord length c . The panel boundaries are then obtained by adding and subtracting the half-thickness of the section at right angles to the mean line. This concentrates the elements at the leading and trailing edges, where greater resolution is required. This characteristic can be seen from the example shown in Fig. 1.

The general two-dimensional hydrofoil problem does not possess any symmetry which can be used to increase the efficiency of the computation. This would not be an important issue in any case, since two-dimensional calculations use such a small amount of computer time.

The exact influence functions for two-dimensional constant strength source and dipole elements are well known [18]. Unlike three-dimensional applications, where sub-

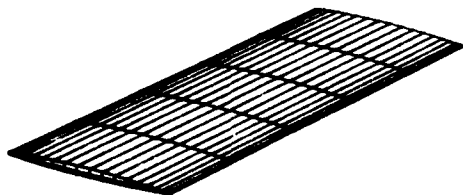


Fig. 1 Chordwise distribution of panels produced by cosine spacing as defined in equation (1). The two-dimensional section has a thickness chord ratio of 5 percent. The number of panels is 40

stantial savings in computing time can be achieved by the use of far field approximations for distant panels, the time savings for a two-dimensional calculation are not worth the trouble.

An approximate Kutta condition for a potential flow panel solution, first introduced by Morino [16], required that the strength of the dipole sheet in the wake be equal to the difference in the value of the dipole strength of the two panels adjacent to the trailing edge. This, combined with the discretized statement of Green's formula given in Appendix 1, results in a system of linear equations for the unknown dipole strengths of each panel. However, J.-T. Lee [17] found that this form of the Kutta condition contained a fundamental error when the free stream contained a component in the direction of a line connecting the control points of the two trailing edge panels. This finding led to a study of the implementation of the Kutta condition for a potential based panel method. The conclusion was that the most accurate and reliable Kutta condition was a requirement of equal pressures on the two trailing edge elements. This is similar to the conclusion reached by Hess [10] for his velocity method. It should be noted, however, that the differences between the results obtained by the original Morino Kutta condition and the present pressure Kutta condition are very small for thin two-dimensional sections. The differences become significant for thick sections and for three-dimensional flows.

This introduces a nonlinear aspect to the solution. However, an iterative scheme can be employed whereby the initial solution is obtained using the original Morino condition, and successive wake dipole strengths are adjusted based on the error in the computed trailing edge element pressures.

The coefficient matrix is unchanged in the process. For the small number of unknowns involved for two-dimensional flows, a Gauss reduction can be used at the outset to decompose the matrix into lower and upper triangular forms for subsequent solutions with different right hand sides. The converged solution for the dipole strengths then represents the distribution of potential around the surface of the hydrofoil.

Surface velocities may then be obtained either by numerical differentiation of the potential, or by direct calculation of the source and dipole panel velocity influence functions. The latter approach is generally not as accurate, since the velocity influence functions are more singular and therefore more sensitive to the position of the control points within each panel. This problem is similar to that of a vortex lattice calculation, where the position of the control points is known to be critical. As a result, numerical differentiation of the potential, with all its inherent dangers, is still the better alternative.

The crudest form of numerical differentiation simply consists of representing the velocity at the panel boundaries as the difference in potential of the two adjacent elements divided by the distance between their centers. A more accurate scheme is to employ either a cubic spline interpolation procedure, or a second-order finite difference method, with arc length along the surface as a parameter. We have chosen this last approach, although we have succeeded in obtaining convergent results with both of the alternatives just discussed.

The final step is the computation of total forces. We know, of course, that for two-dimensional inviscid flow the drag is zero and the lift, from Kutta-Joukowski's law, is $\rho U \Gamma$. Moreover, the circulation, Γ , is equal to the known potential jump or dipole strength in the wake. However,

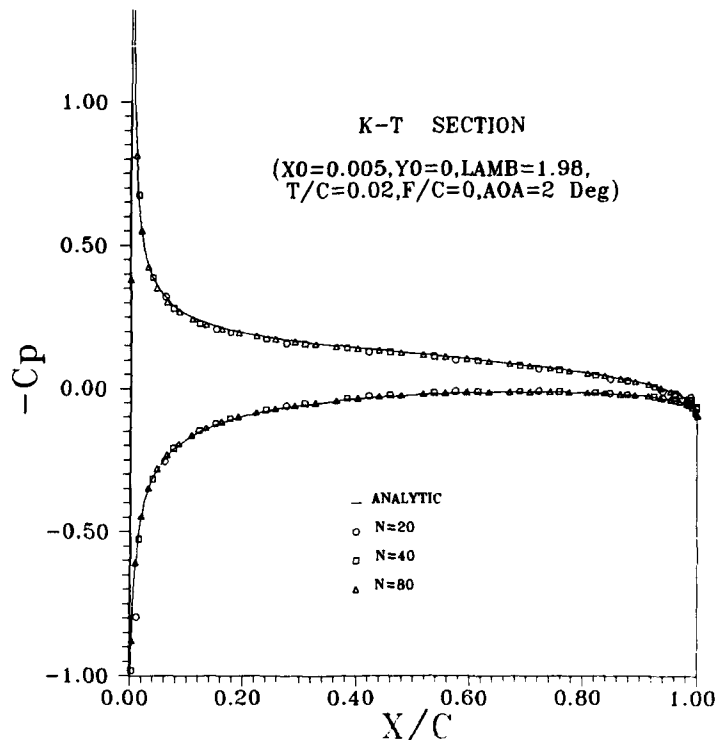


Fig. 2 Chordwise distribution of pressure coefficient C_p for a 2 percent thick symmetrical Karman-Trefftz section at an angle of attack of 2 deg. The trailing edge angle specified in the mapping function is 3.6 deg. Results obtained with the present panel method are given for 20, 40 and 80 panels

to practice for more complicated three-dimensional flows, we will also calculate the force the hard way by integrating the pressure around the section. This can be implemented by multiplying the pressure computed at the midpoint of each panel by the panel arc length, forming a set of N concentrated force vectors in the direction of the surface normals, and adding them up. The error incurred by local pressure integration can then be readily determined.

A typical pressure distribution for a thin section is given in Fig. 2. Results are given for a Karman-Trefftz section whose exact solution can be obtained by conformal mapping [19]. The numerical results are all very close to the exact solution, even with 20 panels. However, 40 panels would probably provide a better definition of the pressure near the leading edge. Results for thicker sections will not be shown here since the agreement between exact and numerical results is even better.

Table 1 provides a comparison of the computed values of lift and drag coefficient obtained by summation of panel forces with exact values obtained by conformal mapping. This is a demanding test since the thin sections develop

very sharp pressure peaks at the leading edge. Using 80 elements, the error in drag is less than 1 percent of the lift. A high level of accuracy can therefore be achieved, but one must be willing to use a large number of panels.

4. The propeller and hub

The problem of grid generation for a propeller blade can be separated into two parts—chordwise spacing and radial spacing. The former is identical to the two-dimensional problem, and we have again adopted cosine spacing, as illustrated in Figs. 3 and 4.

The best choice of the radial distribution of panel size for a propeller blade is not obvious. For the example shown we have used a spacing algorithm which concentrates the elements at the tip. In this case, the radii for M panels are,

$$r_m = R_h + (R - R_h) \sin\left(\frac{\pi}{2M}(m-1)\right),$$

$$m = 1, 2, \dots, M+1 \quad (2)$$

where R_h is the hub radius, R is the tip radius, and M is the number of panels over the radius. For some applications, however, greater resolution near the hub might be desirable, in which case cosine spacing rather than the spacing given in equation (2) might be preferred.

The propeller hub and its intersection with the propeller blades is more complicated. However, we have assumed for the present that the radius of the hub is constant between the leading and trailing edges of the blade, and can be approximated by a quartic function of axial distance

Table 1 Effect of the number of chordwise panels on computed lift and drag coefficient. The exact values are $C_L = 0.223$, $C_D = 0$

N	C_D	C_L
20	0.0061	0.234
40	0.0043	0.229
80	0.0030	0.226

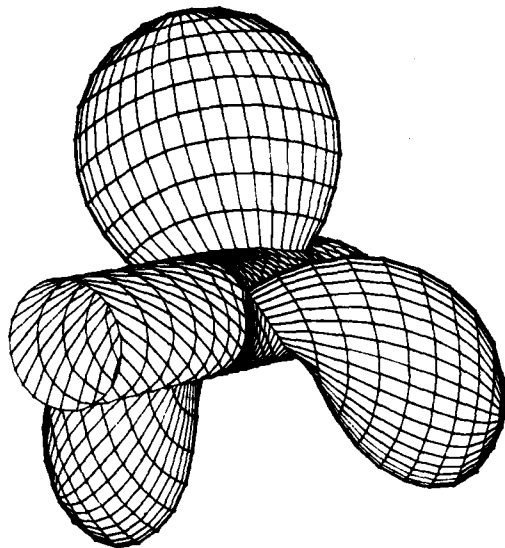


Fig. 3 Panel arrangement viewed from upstream for a three-bladed propeller with a hub. The propeller is DTNSRDC-4118, whose characteristics may be found in [23]

downstream. The upstream portion of the hub is treated as a semi-infinite cylinder. Hub definition, and the hub-blade intersection problem, is then made much easier.

The axial spacing of the panels on the hub matches that of the blade in the interval between the leading and trailing edges, and the circumferential interval along the hub is divided into a prescribed set of equal intervals. This generates a more or less helical pattern of paneling on the hub. The axial coordinates of the intermediate panels must be adjusted, particularly near the leading edge, in order to avoid badly shaped panels in this region. If the axial coordinates were all required to be the same, panels near the leading edge could actually turn inside-out. This arrangement produced some interesting hub pressure distributions which caused us to take a closer look at our hub panel graphics. The result was the addition of an automatic paneling scheme which appears to produce reasonable panel shapes.

The paneling on the hub upstream of the propeller leading edge is purely helical, with a pitch matching the root section pitch of the propeller. The axial spacing is half cosine, with fine spacing near the propeller and coarse spacing upstream. The arrangement on the hub downstream of the trailing edge is similar, except that the pitch is required to match the corresponding pitch of the trailing vortex wake at the hub intersection.

As with any three-dimensional lifting surface, a trailing vortex wake extends downstream from the blades and hub, which must also be paneled with quadrilateral dipole elements. We will use a model for the trailing vortex wake identical to that developed by Greeley and Kerwin [20] for use with a vortex lattice propeller analysis code. Stated briefly, the model divides the wake into a transition wake extending from the trailing edge to a specified distance downstream. In this region, the wake is represented as a discretized vortex sheet with a prescribed contraction shape and an axially varying pitch. The second region, designated the ultimate wake, is modeled more crudely by a single concentrated tip vortex from each blade, and a hub vortex. The quadrilateral dipole panels in the wake

are geometrically identical to the vortex lattice elements used in [20]

We turn next to the question of symmetry. For the steady flow problem, both the geometry and the loading is repeated identically on each blade and on each inter-blade segment of the hub. The number of unknown dipole strengths to be determined is therefore the total number of elements (as seen, for example, in Fig. 3) divided by the number of blades. In fact, the geometry is only determined for one blade, and the influence functions incorporate a built-in summation of the influence of a set of source and dipole panels with angular coordinates incremented by the angle between blades.

This is equivalent to having equal paneling on all blades. Our earlier vortex lattice codes [20, 21] used coarser spacing on the other blades, together with an interpolation scheme to account for their influence on the first, or *key*, blade. However, the panel influence coefficient algorithm which we are using contains an efficient far field approximation which reduces the time required to compute distant elements. Therefore the substantial coding complications required to handle different spacing on other blades was not considered to be necessary in this case.

The influence functions for quadrilateral source and dipole panels are computed using the formulation developed by Newman [22]. The potential is computed exactly for nearby panels, while it is approximated by a multipole expansion for more distant panels. Finally, the panels which are sufficiently distant are treated as point sources and dipoles. This is really the heart of any panel code, and it is essential that the computer code for the influence function be both robust and efficient.

The Kutta condition employed in the propeller problem is logically similar to that used for the two-dimensional hydrofoil. We found that an explicit pressure Kutta condition was particularly necessary near the tip where large radial induced velocities combined with locally swept trailing edges combined to produce inaccurate results. A detailed development of the Kutta condition may be found in Appendix 2.

The resulting system of simultaneous equations is similar to that described for a simple two-dimensional hydrofoil, but the total number of unknowns is much greater. As a result, the time required for a Gauss elimination would start to become prohibitive, and an iterative matrix solver

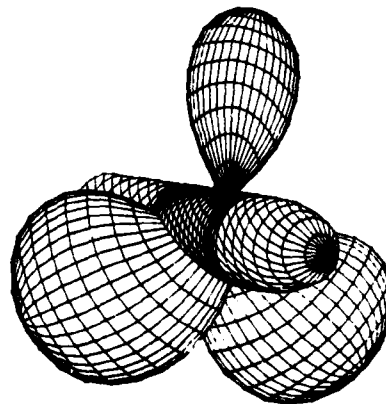


Fig. 4 Panel arrangement viewed from downstream for a three-bladed propeller with a hub. The propeller is DTNSRDC-4118, whose characteristics may be found in [23]

is more efficient. We have employed an accelerated iterative matrix solver following the procedure developed by Clark [23]. While this was developed for use with Hess's velocity based panel codes, we have found that it converges very rapidly for the kind of coefficient matrix encountered with a potential method. For example, the solution for 2000 unknowns, using a DEC Microvax II, takes fifteen minutes, including the time required for external storage and retrieval of the matrix elements. On the other hand, a Gauss reduction, if carried out entirely in memory, would require an estimated time of one hour. Since memory limitations would make the latter option impossible for such a large matrix, external storage would also be required, and the resulting time would be much more than one hour.

The calculation of pressure distributions is again carried out by determining the surface velocity by differentiating the potential. However, in this case a two-dimensional interpolation is required. As shown in Appendix 3, this is accomplished by determining the derivatives of the potential along two nonorthogonal curvilinear coordinates formed by the blade and hub paneling. The magnitude of the velocity is then determined, which can then be used to determine a nondimensional pressure coefficient,

$$C_p = \frac{p - p_\infty}{\frac{\rho}{2} U_\infty^2} \quad (3)$$

Blade pressure distributions at three radii are shown in Fig. 5, while pressure distributions along the hub are shown in Fig. 6.

Finally, the total propeller thrust and torque can be obtained by summation of individual panel force vectors. In order to obtain practically useful results which can be compared with experiments, viscous drag forces are added following the same approximate procedure used in [20]. Tangential force vectors are added in each panel with magnitudes equal to the product of the local dynamic pressure, the panel area and a specified viscous drag coefficient. Thrust and torque coefficients obtained in this way for the sample propeller at several advance coefficients are plotted in Fig. 7 together with experimental results [24]. The agreement appears to be satisfactory in this case.

5. Axisymmetric ducts in uniform flow

The geometry for an axisymmetric duct is particularly simple, since one only needs to specify a meridional section in the same way as a two-dimensional hydrofoil. The chordwise distribution of panels is the same as for the two-dimensional case, while the circumferential paneling is formed from constant angular increments.

For the particular case of uniform inflow, the solution is axisymmetric, so that the number of unknowns is equal to the number of chordwise panels. The influence functions are therefore formed by summing the individual panel contributions circumferentially. All other steps in the solution are carried out in the same way as for a two-dimensional flow.

The first example shown is for a torus, Fig. 8. While this is obviously not a serious candidate for a propeller duct, an analytical solution for the potential was developed in 1893 by Dyson [25]. The analytical solution is developed

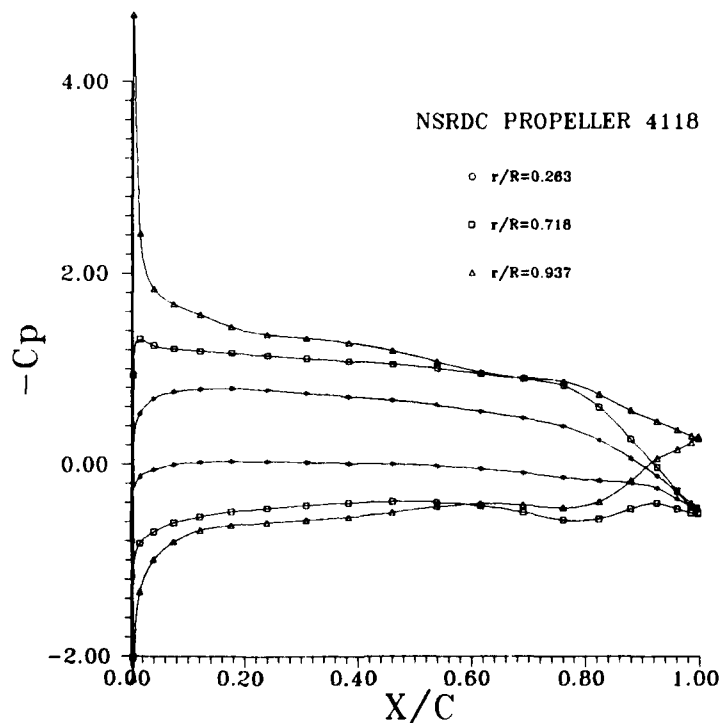
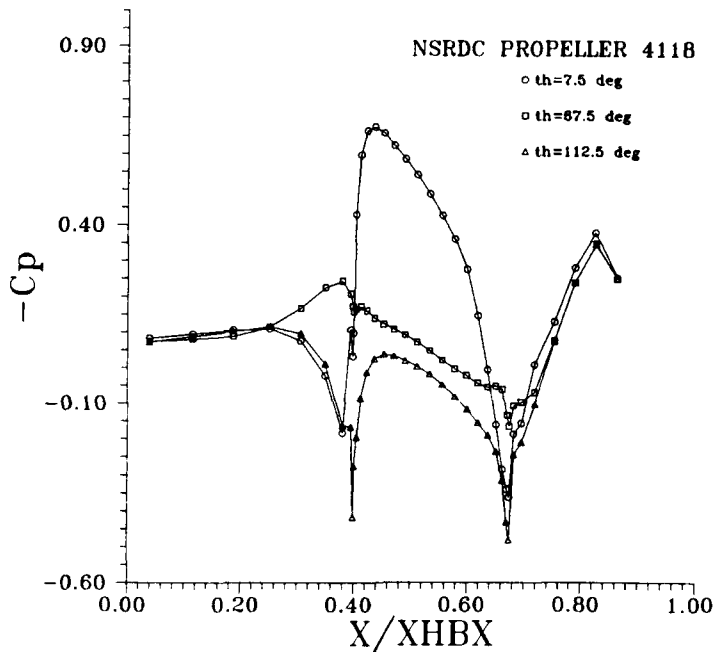


Fig. 5 Computed chordwise pressure distributions for DTNSRDC propeller 4118 operating at an advance coefficient $J = 0.833$. The pressure coefficient in this case is normalized on the uniform advance speed, V_A .



Accession For	
NTIS GRA&I	<input checked="" type="checkbox"/>
DTIC TAB	<input type="checkbox"/>
Unannounced	<input type="checkbox"/>
Justification	
By _____	
Distribution/	
Availability Codes	
Dist	Avail and/or Special

Fig. 6 Computed hub pressure distributions for DTNSRDC propeller 4118 operating at an advance coefficient $J = 0.833$. The pressure coefficient in this case is normalized on the uniform advance speed, V_A . The pressure distributions are given along three helical panels between blades

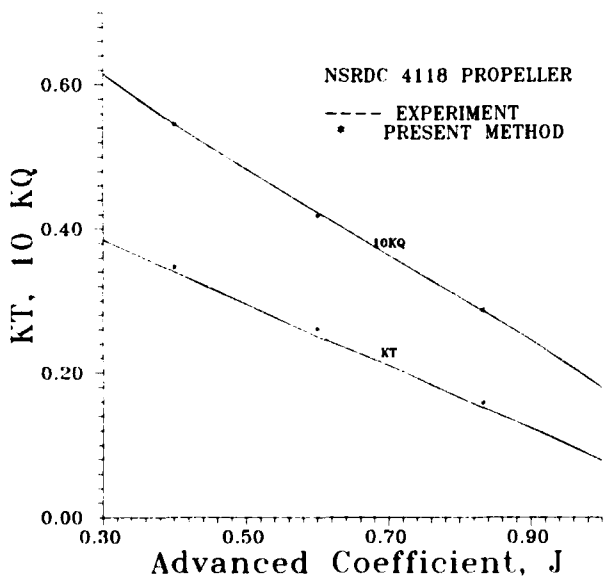


Fig. 7 Comparison of measured and calculated thrust and torque coefficients for DTNSRDC propeller 4118. The experimental results are from [23]. The calculated results are obtained by summation of panel pressures, with viscous effects treated as in [19]

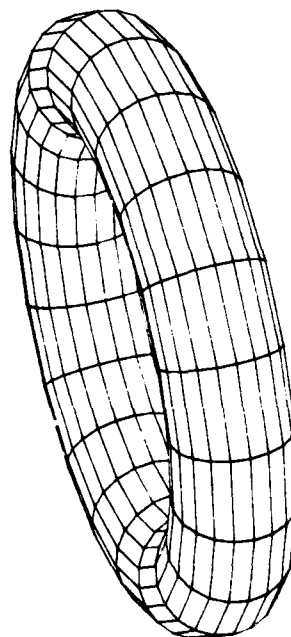


Fig. 8 Panel arrangement for toroidal duct with 20 circumferential and 20 chordwise panels. The ratio of duct cross section radius to mean radius, $r_c/R = 0.25$

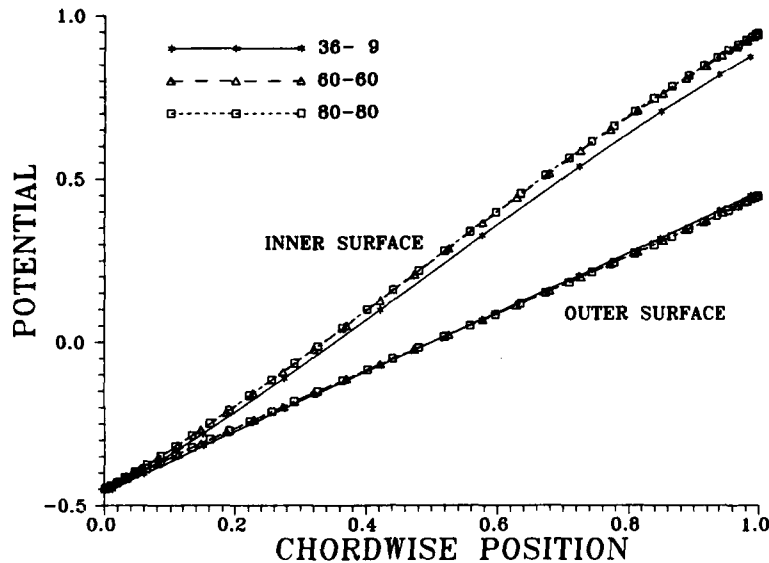


Fig. 9 Distribution of potential over the inner and outer surfaces of a toroidal duct. The exact solution due to Dyson [24] is graphically identical to the 80×80 panel solution

as an expansion in powers of the ratio of the cross-sectional radius, r_c , to mean radius, R , of the torus. Since the circular cross sections of the duct do not possess a natural trailing edge, the circulation is made unique by specifying the angular coordinate of the downstream stagnation point.

Figure 9 shows the computed distribution of potential for different numbers of panels for a torus with $r_c/R = 0.25$. The downstream stagnation point is specified to be at an angular coordinate of zero relative to the axis of the torus.

It is evident that the computed potential distribution over the outer surface is essentially identical for the three grids tested. The result for the inner surface is not converged for the case of 36 chordwise and 9 circumferential panels, but the results for the two finer grids are almost identical. The analytical solution is indistinguishable from the converged numerical results.

The next case is a very long duct formed from an NACA-0010 section set at zero angle of attack on a mean radius of one tenth of the chord. Results for this duct obtained with several panel codes were given by Bristow [26], and additional results were presented by Miranda [27] and by Hess [28] in a discussion to Miranda's paper. Predicting the pressure distribution for such an extreme duct is a very demanding test of a panel code. The mass flow through the duct, which is imposed by the Kutta condition, is extremely high in this case, and there is a tendency for all panel methods to underestimate its value. This is, of course, not a practical issue since viscous effects would completely invalidate the potential flow solution.

Our paneling for this example is shown in Fig. 10, and the pressure distributions for various grids are shown in Fig. 11. The first four calculations are for a fixed number of chordwise panels equal to 36, but with the number of circumferential panels varying between 9 and 60. The results for 36 and 60 circumferential panels are almost identical, and indicate a minimum pressure coefficient of -11.3 . Increasing the number of chordwise elements to 60 reduces the minimum pressure coefficient to -12.5 .

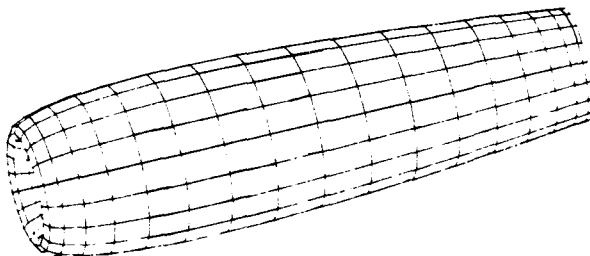


Fig. 10 Panel arrangement for nacelle formed from an NACA 0010 section with a chord/mean radius ratio of 10. There are 36 chordwise and 18 circumferential panels in this illustration

Some results obtained with other panel codes are shown in Fig. 12, which is taken from [27]. The "exact" solution, obtained with a special high order axisymmetric panel code [29] shows a minimum pressure coefficient of -13.8 which is slightly lower than the minimum value which we obtained. The results obtained by a high order panel code developed by Hess [30], and by the QUADPAN [27] low order potential based code, are similar to ours. The results obtained by the Hess low order velocity based code [31] show pressure minima much closer to zero, which is evidently an inherent problem with that method for internal flows.

The next example is a duct with proportions which are more typical for a ducted propeller application. The duct section is again an NACA-0015, but the duct radius at the leading edge is now equal to the duct chord. The duct sections are set at an angle of attack of 10 deg. The grid for this duct is shown in Fig. 13 and pressure distributions are shown in Fig. 14 for varying numbers of panels. Comparing this with Fig. 11 we see that the results are much more convergent. An additional measure of accuracy is the computed drag coefficient, which should be zero in this case. Table 2 gives the values of drag obtained in this case for different numbers of panels. The computed drag

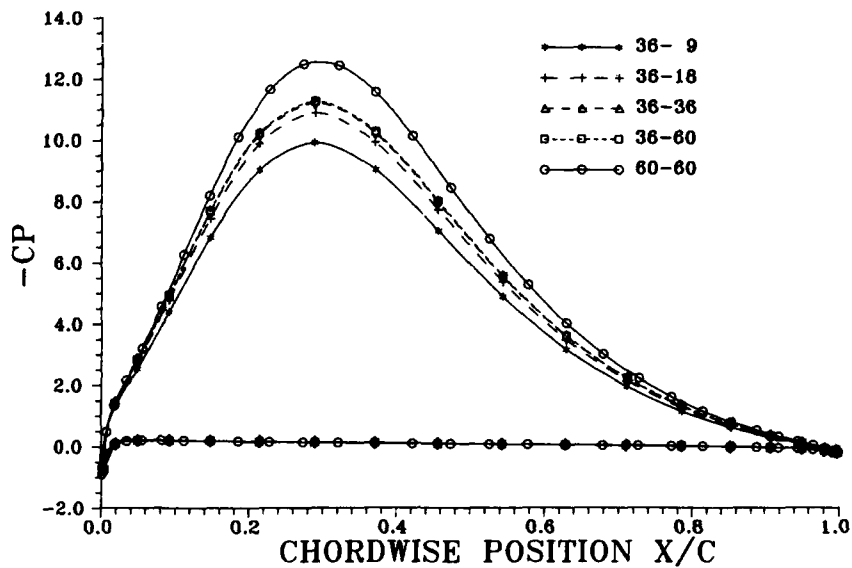


Fig. 11 Pressure distributions for nacelle obtained with the present panel code with different panel arrangements

becomes smaller as the number of panels is increased, and it is somewhat a matter of judgment to set an acceptable value for the drag error. If this duct were to operate with a propeller, the drag error resulting from a 60×60 grid would be on the order of 3 percent of the duct thrust, or less than 1 percent of the total duct and propeller thrust.

6. Ducted propellers

We now turn, finally, to the problem of the ducted propeller. The duct and hub will be considered logically as one unit with axisymmetric geometry. The propeller blades, however, are represented by a vortex lattice using a modification of the procedure described in [20]. This was done in order to reduce the total number of panels required in the solution, and would seem justified on the basis that the tip sections of a propeller are generally much thinner than the duct. However, we plan in the future to provide for the additional alternative of representing the blades by surface panels as described earlier.

The procedure works as follows: The flow around the combination of the axisymmetric hub and duct is first computed, using exactly the same method as for the duct alone. The velocity induced by the hub and duct is then computed as a set of field points in the interior of the duct whose coordinates correspond to the positions of the control points in the vortex lattice representation of the propeller blades. The strengths of the vortex lattice elements on the propeller blades are now computed for this particular spatially varying inflow field based on the requirement that the total normal velocity vanish at each of the control points.

The perturbation potential induced by the propeller

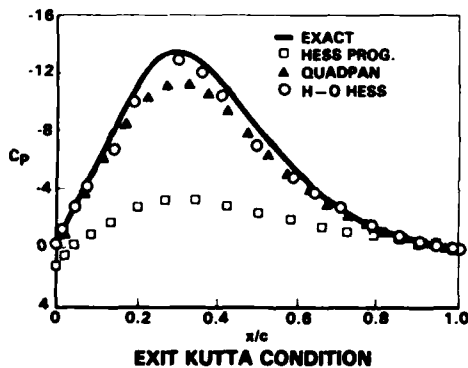


Fig. 12 Pressure distributions for nacelle obtained by different panel methods as presented by Miranda [26]

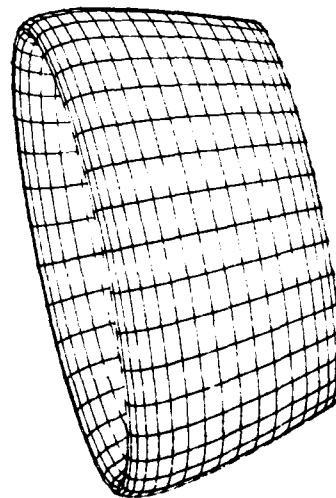


Fig. 13 Panel arrangement for a duct formed from an NACA 0015 section with a chord/leading edge radius ratio of 1. The duct sections are set at an angle of attack of 10 deg

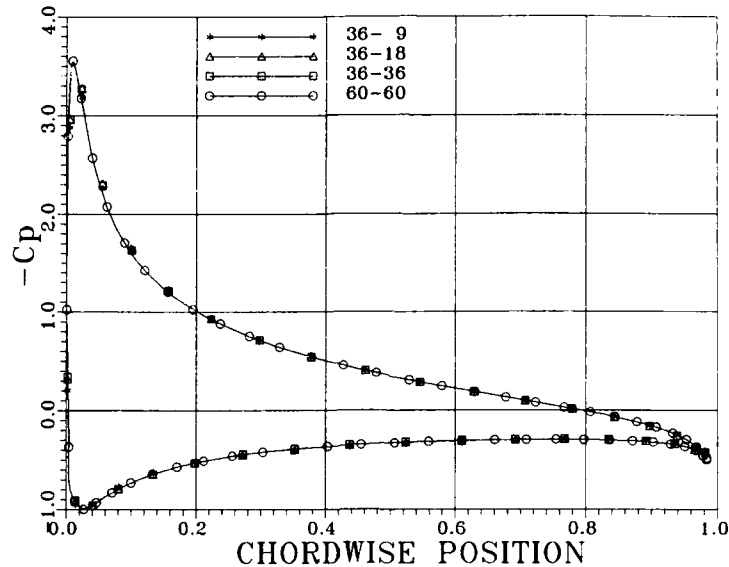


Fig. 14 Pressure distributions for duct illustrated in Fig. 13 obtained by the present panel method with different numbers of elements

blades can now be computed at the centroid of each of the panels on the duct and hub. This modifies the right-hand side of the equations determining the dipole strengths on the hub and duct, and a new solution for the latter is obtained. At this point the flow around the duct and hub is not longer axisymmetric.

New field point velocities induced by the duct and hub on the propeller are then computed, and the propeller solution is repeated. The iterations continue until the changes to both the duct and hub and to the propeller are within a prescribed tolerance. This is generally accomplished within five or six iterations, as will be shown later for a specific example.

Substantial complications arise in this problem as a result of the need for compatibility between the grids on the duct and hub and on the blades. For example, if the panels on the duct lie in meridional planes, as was the case for the axisymmetric problem, the duct grid would intersect the tip panels of the propeller blades and their trailing vortex wakes. The panels on the duct and hub are therefore helical, and exactly match the blade and trailing vortex grid at the tip and at the hub.

This seemed, superficially, to be just a matter of geometry which should not be too difficult to handle. We therefore embarked on a necessary test of the numerics, in which we calculated an axisymmetric duct in uniform flow using panels set at varying pitch angles. The resulting chordwise pressure distribution should, of course, be unchanged.

Table 2 Effect of the number of panels on the computed drag of an axisymmetric duct in inviscid flow. The area used in defining the drag coefficient in this case is half of the total wetted surface area of the duct. The exact value of the drag coefficient is zero

N	M	C_D
36	9	0.0125
36	18	0.0081
36	36	0.0070
60	60	0.0026

Our initial results, on the contrary, showed erratic behavior and poor convergence as the pitch angle of the duct paneling was decreased. This turned out to be due to two effects—the first being the fact that helical panels become very nonplanar as the pitch is decreased. This is very evident from a comparison of Fig. 13 and Fig. 15. The solution to this part of the problem was to divide the quadrilateral panels into pairs of triangular panels, each with the same uniform source and dipole strength. The number of unknowns was therefore the same as with quadrilateral panels.

The second effect was the sensitivity of the potential to the radial position of the control point on the nonplanar panels. We found that the best position could be found from the following simple argument. Suppose that we wanted to compute the surface potential induced by a

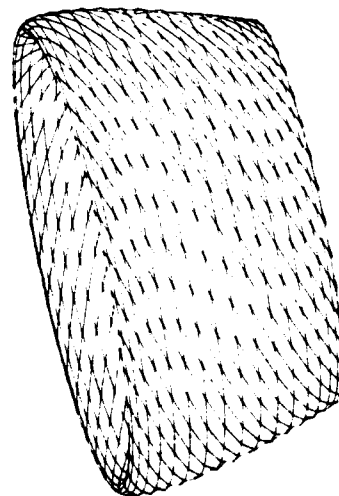


Fig. 15 Panel arrangement for the duct shown in Fig. 13, but with helical paneling with a pitch angle of 20 deg

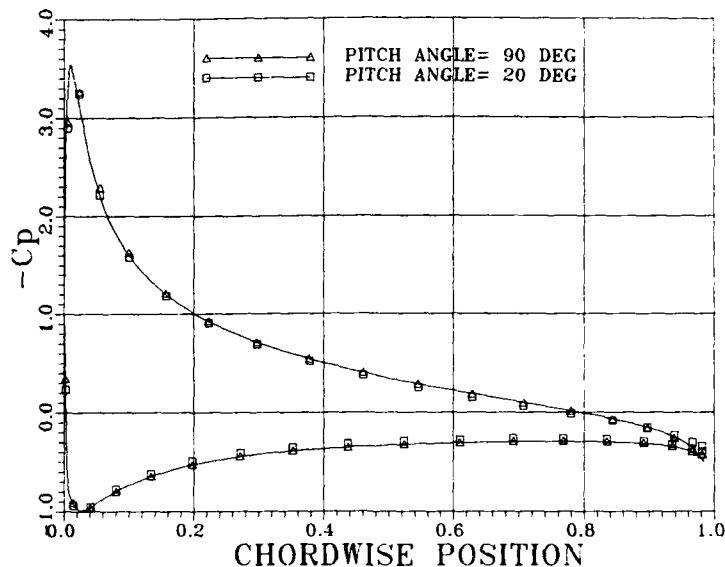


Fig. 16 Comparison of the pressure distributions obtained with panels oriented with 90-deg pitch as shown in Fig. 13 and with panels at 20-deg pitch as shown in Fig. 15

uniform distribution of normal dipoles located on the segment of a cone between two planes normal to its axis. A discretized version of this problem is represented by any one of the circumferential strips on the duct surface shown in Fig. 13. In this case the best positions for the control points are at the centroids of the planar quadrilaterals approximating the conic surface. In particular, the radius of a control point is less than the radius of the true surface.

But we also know that the dipole panels in the discretized problem are equivalent to vortex quadrilaterals, and that in the axisymmetric case the meridional elements cancel. We are therefore left with ring vortices at each end, which in the discretized problem are approximated by polygons.

Finally, we recognize that the same conclusion holds for helical panels. The potential induced at a *fixed point* will be unchanged if the rings are connected by helical lines of arbitrary pitch and the problem is reformulated in terms of dipole panels. Thus we conclude that the correct radial location of the control point is at the centroid of the equivalent planar meridional panel.

The numerical justification for this argument may be found in Fig. 16, where it can be seen that the pressure distributions obtained with 90-deg and 20-deg pitch angles are nearly identical. We have found this to be true for several different duct geometries which we have explored, whereas the results obtained with other choices of position of the control points were not nearly as satisfactory.

Additional geometrical manipulations are required to provide compatibility between the propeller and duct grids. The propeller blade tip, and its extension into the trailing vortex wake downstream, is adjusted to follow the interior contour of the duct with a prescribed radial gap. Finally, the axial spacing on the hub and duct is determined in such a way as to match the grid on the blade. This requires cosine spacing on the interior of the duct from the propeller leading edge to trailing edge. Two

additional regions of cosine spacing are introduced, extending from the duct leading edge to the leading edge of the propeller, and from the propeller trailing edge to the trailing edge of the duct. Finally, the propeller trailing vortex wake grid is adjusted to match the axial spacing on the duct and on the duct wake. This arrangement is similar to that developed by Van Houten [4] for use with his vortex lattice ducted propeller code.

The final result is the panel extravaganza depicted in Fig. 17. The propeller shown has five blades, and a nominal pitch/diameter ratio of 1.4. The blade outline is similar to that employed in the Wageningen KA series [32]. However, to simplify its geometrical description, both the duct and propeller are derived from a single thickness form and mean line with maximum thickness and camber matching those of the actual KA series. Following common

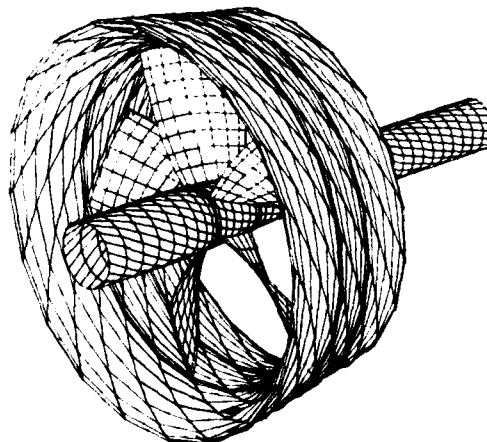


Fig. 17 Panel arrangement for a propeller, hub and duct

practice, we have used a DTNSRDC modified NACA-66 thickness form [33] and an NACA $a = 0.8$ mean line [34].

Since the loading on the duct is not circumferentially uniform, the wake dipole sheet must also vary in strength. A helical pattern for the duct wake is assumed, and the pitch of this wake matches the tip vortex pitch of the propeller. For the present, we have suppressed the contraction of the propeller tip vortex. The duct wake proceeds downstream with a constant radius equal to that of the duct trailing edge, and the propeller tip vortex proceeds downstream with the same radius reduced by the tip gap. This is obviously an idealization since the vortex systems from the propeller and duct must actually interact in a very complicated way. However, it is assumed that this wake model will yield reasonably realistic values of induction on the propeller and duct.

For the steady flow problem, the loading on each blade and on each inter blade sector of the hub and duct is the same. Thus, as with the propeller, the number of unknowns is equal to the total number of blade, duct and hub panels divided by the number of blades. In addition, an important symmetry exists due to the axisymmetric geometry of the duct and hub. If the angular spacing of the panels on both the hub and duct is uniform and equal, the influence coefficients will depend only on the difference in the indices identifying the helical strip containing the panel and containing the control point. This reduces the number of influence coefficients to be computed by a factor of the number of circumferential panels between blades. Since this number needs to be on the order of 10 or 20, the reduction in computing time and storage is substantial.

In order to take advantage of this symmetry, the number of circumferential panels on the duct and hub must be equal. This may result in finer spacing than necessary on the hub, but the overall reduction in computing time introduced by this symmetry far outweighs the time which

would be saved by removing a few circumferential panels on the hub.

As with the propeller panel code, an accelerated iterative matrix solver is used for the duct and hub solution. The velocity induced by the duct and hub at the propeller control points is then computed directly from the panel influence functions. This approach is accurate since most of the field points are far from the duct and hub in terms of panel dimensions, and the nearest points are located on a properly aligned grid.

7. Ducted propeller results

We will next discuss some of the results obtained for the ducted propeller illustrated in Fig. 17. Following the conclusions of Appendix 4, we have made calculations for two extreme limits of the tip gap—a gap of 4 percent of the radius, for which a potential flow model of the tip and the hub is reasonably valid, and zero gap, where no gap flow exists.

Figure 18 shows how the iterations between the duct and blade solution converge in the case of the 4 percent gap. The first estimate of the radial distribution of circulation on the blades is high, since at this stage none of the propeller circulation has been transferred to the duct. In the second iteration, the duct circulation induced by the propeller has resulted in increased flow speed through the duct, thus decreasing the loading on the blades. This effect is slightly overestimated, since the first iteration blade loading was too high. By the third iteration, the results have practically converged, and almost no difference can be seen in the figure between the fourth and seventh iterations. The same pattern exists for the solution on the duct.

Some indications of sensitivity to numbers of panels is given in Figs. 19 and 20. The first shows the circumfer-

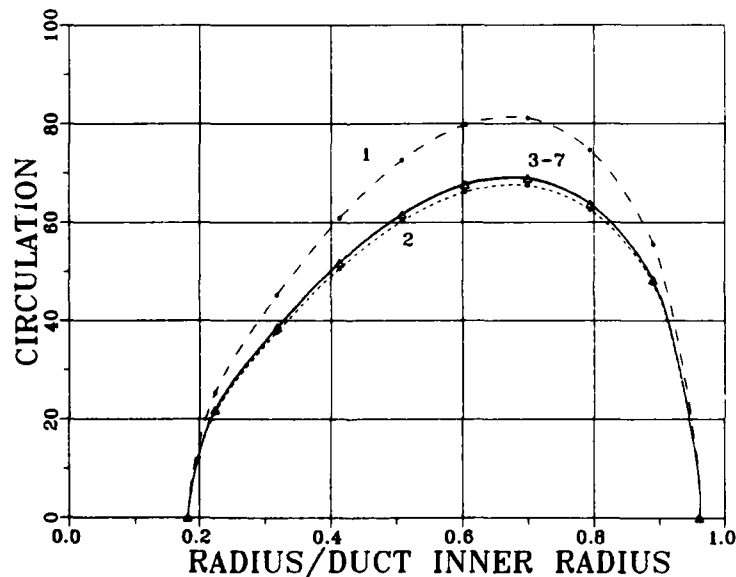


Fig. 18 Illustration of the iterative procedure used to obtain the duct and blade solutions. The circulation distribution on the blade obtained for each of seven iterations is shown

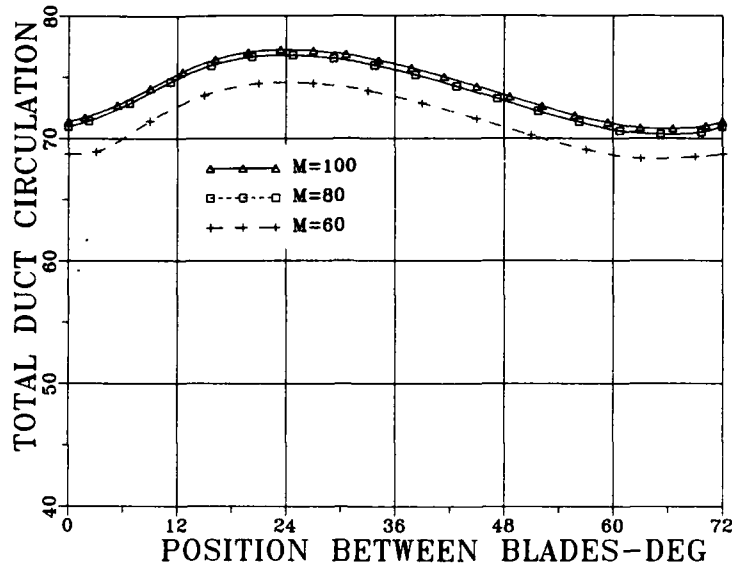


Fig. 19 Example of the influence of numbers of panels on the calculated circulation on the duct

ential variation in total circulation on the duct obtained with different numbers of chordwise and circumferential panels. The two finest spacings produce nearly identical results, while the coarsest spacing yields results which are about 3 percent low. Figure 20 shows the chordwise pressure distribution on the duct for one of the panels closest to the blade tip. The differences in pressure distribution obtained with 60, 80 and 100 panels is due principally to the fact that the actual position on the duct moves closer to the blade tip as the number of panels is increased.

Figure 21 shows the radial distribution of circulation on the blades for zero and 4 percent gap, and the trends near the blade tip are as expected. The fact that the maximum circulation increases as the gap is increased is evidently a result of the coupling of the blade and duct circulation altering the mean flow speed through the duct. Figure 22 shows the effect of advance coefficient on the radial distribution of circulation on the blades for the case of zero gap.

Figure 23 shows the effect of the gap on the circum-

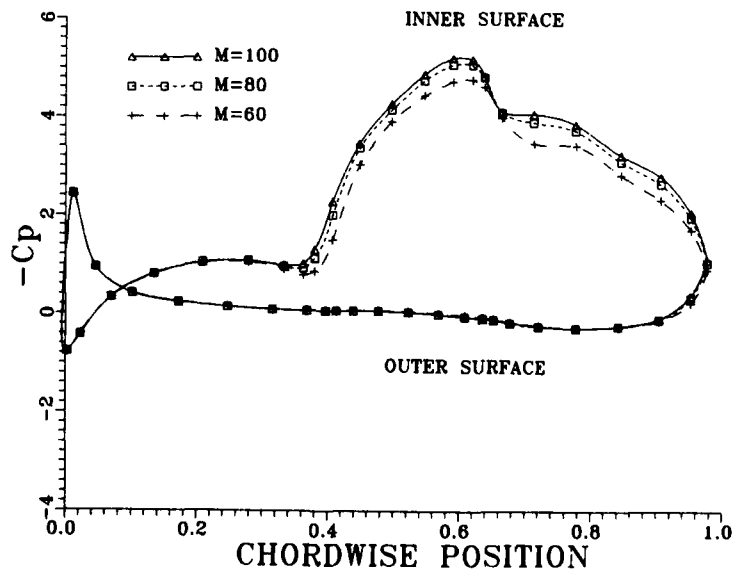


Fig. 20 Example of the influence of numbers of panels on the calculated pressure distribution on the duct

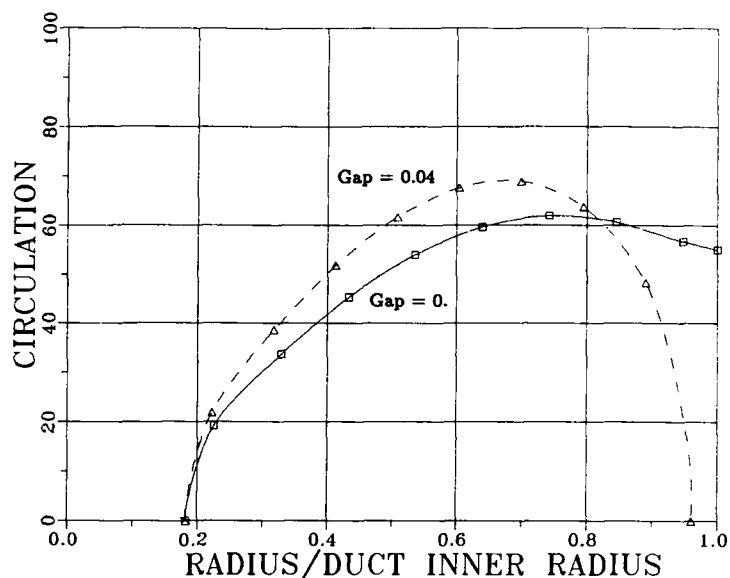


Fig. 21 Influence of tip gap on the radial distribution of circulation on the blades

ferential distribution of circulation on the duct. Decreasing the gap from four percent to zero greatly increases the mean circulation, as well as its circumferential variation. In addition, the zero gap case shows a discontinuity in circulation at the blade tip, which is reasonably close to the value of the finite circulation at the blade tip.

We turn next to detailed flow distributions on the blade and duct. Figure 24 shows the chordwise distribution of

circulation on the blades at a sequence of positions over the radius. The blades are evidently operating with considerable angle of attack loading in this condition.

Finally, Figs. 25 and 26 show the chordwise pressure distributions on the duct for each of the helical strips of panels between a pair of blades. In the case of the 4 percent gap, the pressure minimum is near the blade tip, but is continuous in passing across the blade tip. On the other

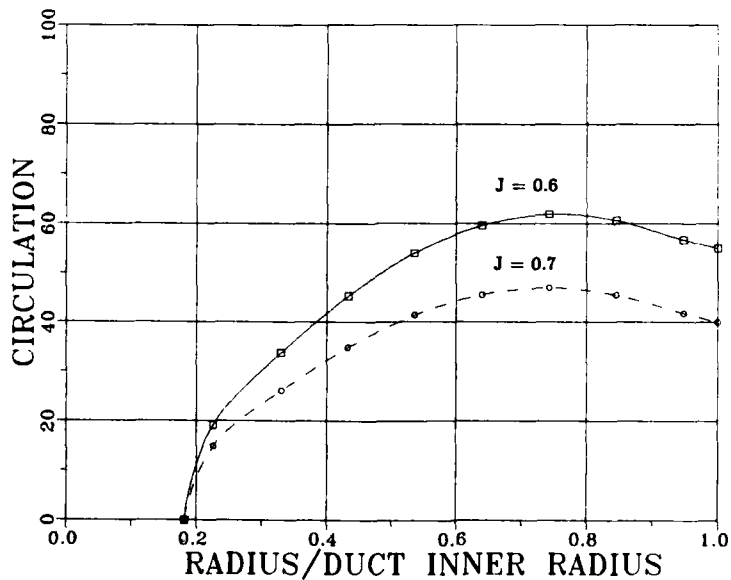


Fig. 22 Influence of advance coefficient on the radial distribution of circulation on the blades

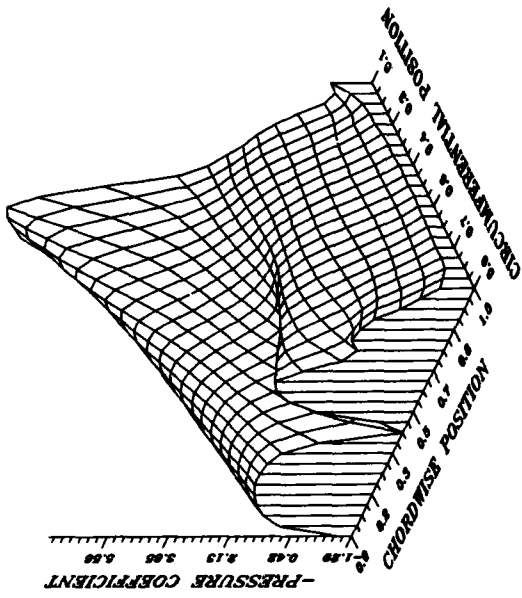


Fig. 25 Pressure distribution on the interior surface of the duct for the case of $J = 0.6$ and zero tip gap. The circumferential coordinate is defined as 0.0 at the intersection of the duct and the suction side of one propeller blade, and 1.0 at the intersection of the duct and the pressure side of the next blade

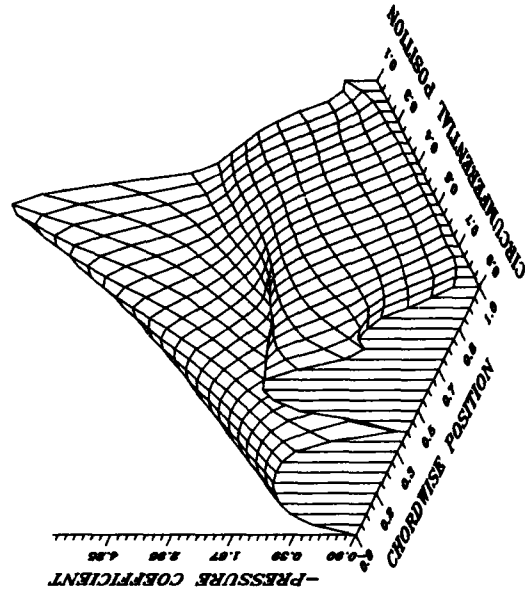


Fig. 26 Pressure distribution on the interior surface of the duct for the case of $J = 0.7$ and zero tip gap. The coordinates are the same as in Fig. 25

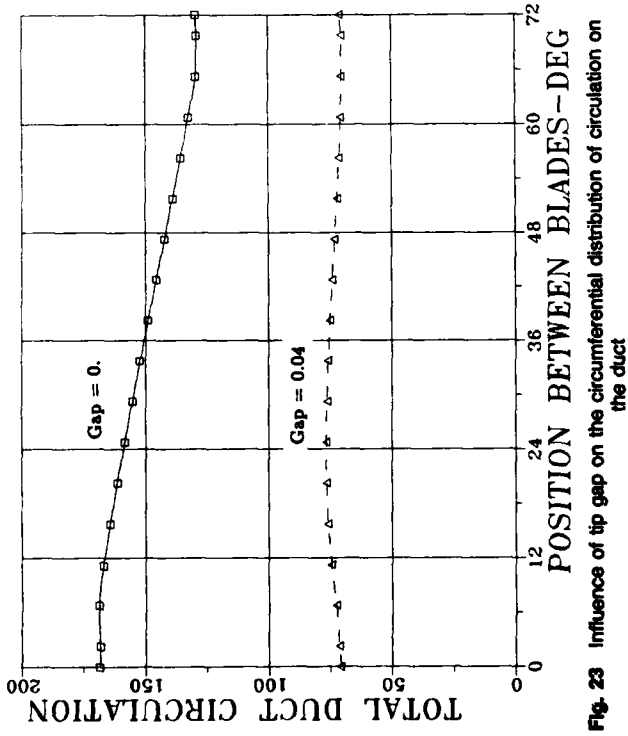


Fig. 23 Influence of tip gap on the circumferential distribution of circulation on the duct

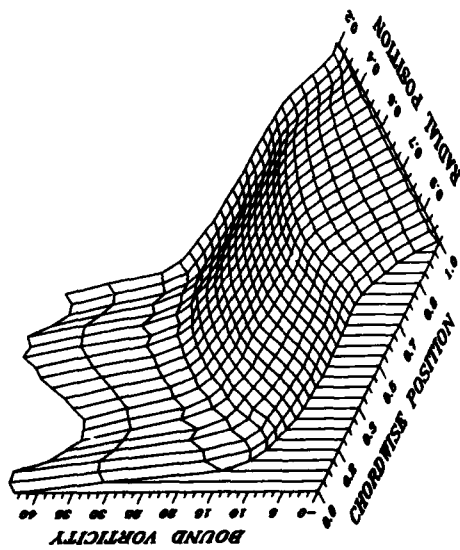


Fig. 24 Chordwise circulation distributions on the blade at an advance coefficient $J = 0.6$ with zero tip gap

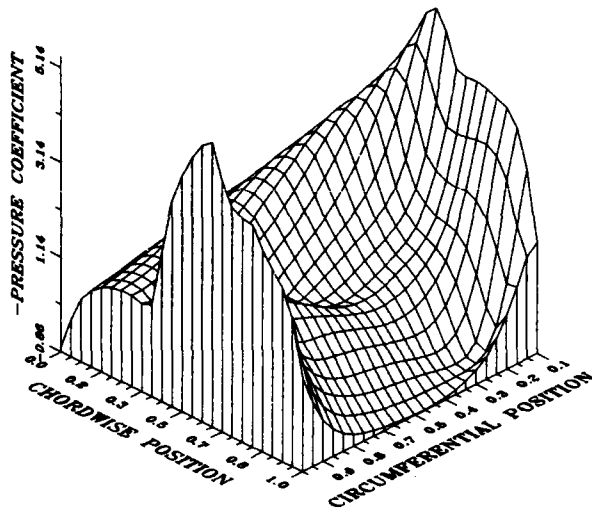


Fig. 27 Pressure distribution on the interior surface of the duct for the case of $J = 0.6$ and 4 percent tip gap. The coordinates are the same as in Fig. 26

hand, with zero gap, the pressure minimum on the duct is on the suction side of the blade tip, and the pressure coefficient is discontinuous across the tip. This discontinuity is, of course, related to blade loading as evidenced by the difference between Figs. 27 and 26. The calculated total propeller and duct forces for these cases are given in Table 3.

8. Acknowledgment

The work described in this paper was carried out under the sponsorship of the Office of Naval Research Accelerated Research Initiative in Ship Hydrodynamics.

References

- Gibson, I. S. and Lewis, R. I., "Ducted Propeller Analysis by Surface Vorticity and Actuator Disc Theory" in *Proceedings, Symposium on Ducted Propellers*, The Royal Institution of Naval Architects, Teddington, England, May 1973.
- Glover, E. J. and Ryan, P. G., "A Comparison of the Theoretical and Experimental Performance of a Ducted Propeller System" in *Proceedings, Symposium on Ducted Propellers*, The Royal Institution of Naval Architects, Teddington, England, May 1973.
- Falcão de Campos, J. A. C., "On the Calculation of Ducted Propeller Performance in Axisymmetric Flows," Technical Report 696, Netherlands Ship Model Basin, Wageningen, the Netherlands, 1983.
- Van Houten, R., "Analysis of Ducted Propellers in Steady Flow," Technical Report 4.76-1, Airflow Research and Manufacturing Corp., Watertown, Mass., Feb. 1986.
- Feng, J. and Dong, S., "A Method for the Prediction of Unsteady Hydrodynamic Performance of the Ducted Propeller With a Finite Number of Blades," Technical Report 85006, China Ship Scientific Research Center, Wuxi, China, Aug. 1985.
- Lakshminarayana, B., "Methods of Predicting the Tip Clearance Effects in Axial Flow Turbomachinery," *Trans. ASME*, Sept. 1970, pp. 476-482.
- Booth, T. S., Dodge, P. R., and Hepworth, H. K., "Rotor-Tip Leakage: Part 1—Basic Methodology," *ASME Journal of Engineering for Power*, Vol. 104, Jan. 1982, pp. 154-161.
- McBride, M. W., "The Design and Analysis of Turbomachinery in an Incompressible Steady Flow Using the Streamline Curvature Method," Technical Report TM 79-33, The Pennsylvania State University, University Park, Pa., Feb. 1979.
- Hess, J. L. and Smith, A. M. O., "Calculation of Nonlifting

Table 3 Computed thrust and torque coefficients for the ducted propeller examples

GAP	J	K_T (PROP)	K_Q (PROP)	K_T (DUCT)
0.04	0.6	0.320	0.0761	0.049
0.00	0.6	0.352	0.0842	0.129
0.00	0.7	0.311	0.0755	0.097

Potential Flow About Arbitrary Three-Dimensional Bodies," *Journal of Ship Research*, Vol. 8, No. 2, Sept. 1964.

10 Hess, J. L., "Review of Integral-Equation Techniques for Solving Potential-Flow Problems with Emphasis on the Surface-Source Method," *Computational Methods in Applied Mechanics and Engineering*, Vol. 5, 1975, pp. 145-196.

11 Hunt, B., "The Mathematical Basis and Numerical Principles of the Boundary Integral Method for Incompressible Potential Flow over 3-D Aerodynamic Configurations" in *Numerical Methods in Applied Fluid Dynamics*, Academic Press, New York, 1980, pp. 49-135.

12 Margason, J., Kjelgaard, S. Q., Sellers, W. L., Morris, C. E. K., Walkey, K. B., and Shields, E. W., "Subsonic Panel Methods—A Comparison of Several Production Codes" in *Proceedings, AIAA 23rd Aerospace Sciences Meeting*, Reno, Nev., Jan. 1985.

13 Maskew, B., "Prediction of Subsonic Aerodynamic Characteristics: A Case for Low-Order Panel Methods," *Journal of Aircraft*, Vol. 19, No. 2, Feb. 1982, pp. 157-163.

14 Youngren, H. H., Bouchard, E. E., Coopersmith, R. M., and Miranda, L. R., "Comparison of Panel Method Formulations and Its Influence on the Development of QUADPAN, an Advanced Low Order Method," in *Proceedings, AIAA Applied Aerodynamics Conference*, Danvers, Mass., July 1983.

15 Hess, J. L. and Valarezo, W. O., "Calculation of Steady Flow About Propellers by Means of a Surface Panel Method" in *Proceedings, 23rd Aerospace Sciences Meeting, AIAA, Reno, Nev., Jan. 1985*.

16 Morino, L. and Kuo, C.-C., "Subsonic Potential Aerodynamics for Complex Configurations: A General Theory," *AIAA Journal*, Vol. 12, No. 2, Feb. 1974, pp. 191-197.

17 Lee, J.-T., "A Potential Based Panel Method for The Analysis of Marine Propellers in Steady Flow," Ph.D. thesis, M.I.T., Department of Ocean Engineering, Cambridge, Mass., Aug. 1987.

18 Moran, J., *An Introduction to Theoretical and Computational Aerodynamics*, Wiley, New York, 1984.

19 Durand, W. F., *Aerodynamic Theory*, Dover, New York, 1963.

20 Greeley, D. S. and Kerwin, J. E., "Numerical Methods for Propeller Design and Analysis in Steady Flow," *TRANS. SNAME*, Vol. 90, 1982.

21 Kerwin, J. E. and Lee, C.-S., "Prediction of Steady and Unsteady Marine Propeller Performance by Numerical Lifting-Surface Theory," *TRANS. SNAME*, Vol. 86, 1978.

22 Newman, J. N., "Distributions of Sources and Normal Dipoles Over a Quadrilateral Panel," *Journal of Engineering Mathematics*, Vol. 20, 1986, pp. 113-126.

23 Clark, R. W., "A New Iterative Matrix Solution Procedure for Three-Dimensional Panel Methods" in *Proceedings, 23rd Aerospace Sciences Meeting, AIAA, Reno, Nev., Jan. 1985*.

24 Boswell, R. J. and Miller, M. L., "Unsteady Propeller Loading—Measurement, Correlation, with Theory and Parametric Study," DTNSRDC Technical Report 2625, David W. Taylor Naval Ship Research and Development Center, Oct. 1968.

25 Dyson, F. W., "The Potential of an Anchor Ring," *Philosophical Transactions*, 1893.

26 Bristow, D. R. and Grose, G. G., "Modification of the Douglas Neumann Program to Improve the Efficiency of Predicting Component Interference and High Lift Characteristics," NASA Technical Report CR-3020, Langley Research Center, National Aeronautics and Space Administration, 1978.

27 Miranda, L. R., "Application of Computational Aerodynamics to Airplane Design," *Journal of Aircraft*, Vol. 21, June 1984, pp. 355-370.

28 Hess, J. L., "Comment on Application of Computational Aerodynamics to Airplane Design," *Journal of Aircraft*, Vol. 22, No. 4, April 1985, pp. 351-352.

29 Carmichael, R. L. and Erickson, L. L., "Pan Air—A Higher Order Panel Method for Predicting Subsonic and Supersonic Linear Potential Flows About Arbitrary Configurations," *AIAA Paper*

81-0252, American Institute of Aeronautics and Astronautics, 1981.

30 Heas, J. L., "An Improved Higher Order Panel Method for Three-Dimensional Lifting Potential Flow," NADC Technical Report 79277-60, Naval Air Development Center, Dec. 1981.

31 Heas, J. L., "Calculation of Potential Flow About Arbitrary Three-Dimensional Lifting Bodies," Technical Report MDC J5678-01, McDonnell Douglas Corp., Oct. 1972.

32 Van Manen, J. D., "Effects of Radial Load Distribution on the Performance of Shrouded Propellers," *Trans.*, The Royal Institution of Naval Architects, 1962.

33 Brockett, T., "Minimum Pressure Envelopes for Modified NACA-66 Sections with NACA $\alpha = 0.8$ Camber and Buships Type I and Type II Sections," David W. Taylor Naval Ship Research and Development Center Report 1780, Teddington, U.K., Feb. 1966.

34 Abbott, I. H. and Von Doenhoff, A. E., *Theory of Wing Sections*, Dover, New York, 1959.

35 Lamb, H. *Hydrodynamics*, 6th ed., Cambridge University Press, Cambridge, U.K., 1932.

36 Batchelor, G. K., *An Introduction to Fluid Dynamics*, Cambridge University Press, Cambridge, U.K., 1967.

Appendix 1

Review of the basic theory

The basic mathematical theory behind the various panel methods will be summarized and the characteristics of each method will be compared in order to determine the most suitable method for the analysis of marine propellers and ducts. The common basis of the apparently different panel methods will then become evident.

Panel methods can be grouped as follows:

- Potential field formulation:
 - perturbation potential method
 - total potential method.
- Velocity field formulation:
 - mixed source and dipole method
 - dipole method (equivalently, vorticity method)
 - source based method

Statement of the problem

Consider a closed three-dimensional domain V with boundary S , the unit normal vector \vec{n} to S being oriented into V , as shown in Fig. 28. The boundary S is composed of the body surface S_B , the wake surface S_w , and the outer control surface S_∞ surrounding the body and wake surface. The body is subject to the inflow velocity U_∞ . With the assumption that the fluid in V is incompressible, inviscid and irrotational, there exists a perturbation velocity potential ϕ , which satisfies the Laplace equation

$$\nabla^2 \phi = 0 \quad (4)$$

A boundary-value problem can be constructed by specifying boundary conditions on the boundary S as follows:

- The kinematic boundary condition should be satisfied on the solid body surface S_B :

$$\frac{\partial \phi}{\partial n} = -\vec{U}_\infty \cdot \vec{n} \quad (5)$$

- The wake surface S_w is assumed to have zero thickness. The normal velocity jump and the pressure jump across S_w is zero, while a jump in the potential is allowed:

$$(\Delta p)_{\text{on } S_w} = p^+ - p^- = 0 \quad (6)$$

$$\left(\Delta \frac{\partial \phi}{\partial n} \right)_{S_w} = \left(\frac{\partial \phi}{\partial n} \right)^+ - \left(\frac{\partial \phi}{\partial n} \right)^- = 0 \quad (7)$$

For the steady lifting problem, the potential jump across the wake surface is the same as the circulation around the body, and is constant in the streamwise direction on S_w :

$$(\Delta \phi)_{\text{on } S_w} = \phi^+ - \phi^- = \Gamma \quad (8)$$

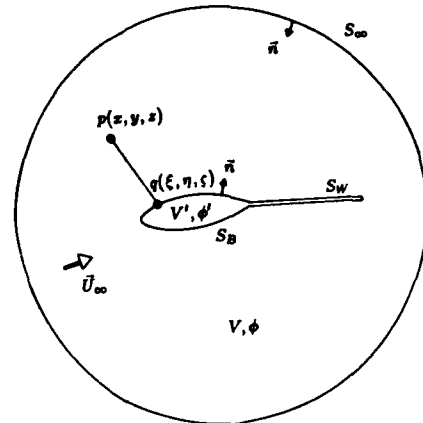


Fig. 28 Notation for a general body for the application of Green's theorem

- A Kutta condition is required at the trailing edge to uniquely specify the circulation. In its most general form, it states that the flow velocity at the trailing edge remains bounded, that is

$$|\nabla \phi|_{TE} < \infty \quad (9)$$

- On the outer control surface S_∞ , the perturbation velocity due to the body should vanish in the limit where this surface is an infinite distance from the body.

$$\nabla \phi \rightarrow 0, \text{ as } S_\infty \rightarrow \infty \quad (10)$$

According to Lamb [35], this boundary-value problem from the velocity potential outside the body surface can be transformed into an integral equation, upon consideration of a fictitious fluid in V' , which is the domain internal to the body surface S_B :

$$4\pi\phi(p) = \iint_{S_B} \left[(\phi(q) - \phi'(q)) \frac{\partial}{\partial n_q} \frac{1}{R(p;q)} - \left(\frac{\partial \phi(q)}{\partial n_q} - \frac{\partial \phi'(q)}{\partial n_q} \right) \frac{1}{R(p;q)} \right] dS + \iint_{S_w} \Delta \phi(q) \frac{\partial}{\partial n_q} \frac{1}{R(p;q)} dS \quad (11)$$

where

- ϕ = perturbation velocity potential in V
- ϕ' = perturbation velocity potential in V'
- $p(x, y, z)$ = field point where induced potential is calculated
- $q(\xi, \eta, \zeta)$ = source point where singularity is located
- $R(p;q)$ = distance between points p and q
 $= \sqrt{(x - \xi)^2 + (y - \eta)^2 + (z - \zeta)^2}$
- $\frac{\partial}{\partial n_q}$ = normal derivative with respect to point q

This equation may be regarded as a representation of the velocity potential in terms of a normal dipole distribution of strength $(\phi - \phi')$ on the body surface S_B , a source distribution of strength $(\partial \phi / \partial n) - (\partial \phi' / \partial n)$ on S_B , and a normal dipole distribution of strength $\Delta \phi$ on the wake surface S_w .

Because the fictitious fluid inside S_B does not have physical meaning, we can choose the internal velocity potential ϕ' to suit our convenience. By choosing a different ϕ' in equation (11), we can formulate a different kind of the panel methods which uses a different set of the singularities.

Potential field formulation

If we choose the fictitious potential as $\phi' = 0$ on S_B , equation (11) for the field point p on the body surface S_B becomes

$$2\pi\phi(p) = \int \int_{S_B} \left[\phi(q) \frac{\partial}{\partial n_q} \frac{1}{R(p;q)} - \frac{\partial\phi(q)}{\partial n_q} \frac{1}{R(p;q)} \right] dS + \int \int_{S_w} \Delta\phi(q) \frac{\partial}{\partial n_q} \frac{1}{R(p;q)} dS \quad (12)$$

Here the surface integral on S_B must be defined to exclude the immediate vicinity of the singular point.

Because $\partial\phi/\partial n$ is known on S_B from the boundary condition, equation (5), equation (12) is a Fredholm integral equation of the second kind for the dipole strength ϕ , which is also the potential value on the body surface S_B . The potential jump across the wake surface can be set to the difference between the potential values of the upper and lower surface at the trailing edge, which replaces the Kutta condition. Discretization of equation (12) will lead to a linear system of equations for the unknown ϕ . The surface velocity, hence the pressure, on S_B can be calculated by a numerical differentiation of the potential distribution. This form of a panel method was first used by Morino [16], and adopted in the present paper. We will refer to this as Morino's method or the perturbation potential method.

If there exists the inflow velocity potential, such that $\nabla\phi_\infty = \vec{U}_\infty$, we can formulate another form of the panel method by choosing the internal potential in equation (11) as a negative of the inflow velocity potential, that is, $\phi' = -\phi_\infty$. The source strength in equation (11) becomes zero because of the boundary condition, equation (5), while the dipole strength, which is the difference between ϕ and ϕ' , becomes the total potential

$$\phi - \phi' = \phi + \phi_\infty \equiv \Phi \quad (13)$$

As the point p approaches the body surface S_B , the contribution from the immediate surface S_i on S_B in the first term of equation (11) is

$$\lim_{S_i \rightarrow 0} \lim_{r \rightarrow S_B} \int_{S_i} (\phi - \phi') \frac{\partial}{\partial n_q} \frac{1}{R(p;q)} dS = 2\pi(\phi - \phi') = 2\pi\Phi \quad (14)$$

The resulting equation is

$$2\pi\Phi(p) = 4\pi\phi_\infty(p) + \int \int_{S_B} \Phi(q) \frac{\partial}{\partial n_q} \frac{1}{R(p;q)} dS + \int \int_{S_w} \Delta\Phi(q) \frac{\partial}{\partial n_q} \frac{1}{R(p;q)} dS \quad (15)$$

This equation can be regarded as a representation of the total velocity potential in terms of a normal dipole distribution only on the body surface S_B and the wake surface S_w . Given the inflow velocity potential values, this is also a Fredholm integral equation of the second kind for the total potential Φ . Discretization of this equation gives another form of panel method, which we will refer to as the total potential method.

Velocity field formulation

Instead of forming an integral equation in the potential field, we can alternatively construct one in the velocity field. Take a normal derivative of equation (11) with respect to the field point p ; then the resulting equation when the field point p is on S_B is

$$4\pi \frac{\partial\phi(p)}{\partial n_p} = 2\pi\sigma(p) + \int \int_{S_B} \sigma(q) \frac{\partial}{\partial n_p} \left(\frac{-1}{R(p;q)} \right) dS + \int \int_{S_B} \mu(q) \frac{\partial^2}{\partial n_p \partial n_q} \frac{1}{R(p;q)} dS + \int \int_{S_w} \Delta\phi(q) \frac{\partial^2}{\partial n_p \partial n_q} \frac{1}{R(p;q)} dS \quad (16)$$

where

$$\sigma = \frac{\partial\phi}{\partial n} - \frac{\partial\phi'}{\partial n} \quad \text{and} \quad \mu = \phi - \phi'$$

Because the velocity induced by the dipole distribution is equivalent to that induced by a vorticity distribution on the same surface with strength $\vec{\gamma}$, which is calculated as a vector product of the normal vector and the local surface gradient of the dipole strength [11], we can write alternatively:

$$4\pi \frac{\partial\phi(p)}{\partial n_p} = 2\pi\sigma(p) + \int \int_{S_B} \sigma(q) \frac{\partial}{\partial n_p} \left(\frac{-1}{R} \right) dS + \int \int_{S_B} \vec{n}_p \cdot \vec{\gamma}(q) \times \nabla_p \left(\frac{-1}{R} \right) dS + \int \int_{S_w} \vec{n}_p \cdot \vec{\gamma}(q) \times \nabla_p \left(\frac{-1}{R} \right) dS \quad (17)$$

where

$$\vec{\gamma} = \vec{n}_q \times \nabla_{z-d}(\phi - \phi')$$

Here again, as we choose a different value for the internal potential ϕ' inside S_B , we can express the normal velocity on S_B in terms of a different set of singularities.

If we choose the internal potential in equation (16) as $\phi' = 0$, it can be shown that $\partial\phi'/\partial n_p = 0$ on S_B ; then

$$2\pi \frac{\partial\phi(p)}{\partial n_p} = \int \int_{S_B} \sigma(q) \frac{\partial}{\partial n_p} \left(\frac{-1}{R} \right) dS + \int \int_{S_B} \mu(q) \frac{\partial^2}{\partial n_p \partial n_q} \frac{1}{R} dS + \int \int_{S_w} \Delta\phi(q) \frac{\partial^2}{\partial n_p \partial n_q} \frac{1}{R} dS \quad (18)$$

where

$$\sigma = \frac{\partial\phi}{\partial n} \quad \text{and} \quad \mu = \phi$$

This can be regarded as the normal induced velocity at p due to the mixed distribution of normal dipoles of strength ϕ , the source distribution of strength $\partial\phi/\partial n$ on S_B and the normal dipole distribution of strength $\Delta\phi$ on S_w . Given the source strength and the left hand side of the equation from the body boundary condition, this is an integral equation of the first kind for the unknown dipole strength μ . Discretization of this equation will give another form of panel method, which we will refer to as the mixed source and dipole method. This can be regarded as the velocity field formulation of the perturbation potential method.

An equivalent formulation derived from equation (17) leads to a mixed distribution of sources and vortices instead of dipoles:

$$2\pi \frac{\partial \phi(p)}{\partial n_p} = \int_{S_B} \sigma(q) \frac{\partial}{\partial n_p} \left(\frac{-1}{R} \right) dS + \int_{S_B} \vec{n}_p \cdot \vec{\gamma}(q) \times \nabla_p \left(\frac{-1}{R} \right) dS + \int_{S_W} \vec{n}_p \cdot \vec{\gamma}(q) \times \nabla_p \left(\frac{-1}{R} \right) dS \quad (19)$$

where

$$\sigma = \frac{\partial \phi}{\partial n} \quad \text{and} \quad \vec{\gamma} = \vec{n}_q \times \nabla_{2-q} \phi$$

If we choose the internal potential as $\partial \phi' / \partial n = \partial \phi / \partial n$, the source strength becomes zero and equation (16) becomes

$$4\pi \frac{\partial \phi(p)}{\partial n_p} = \int_{S_B} \mu(q) \frac{\partial^2}{\partial n_p \partial n_q} \frac{1}{R} dS + \int_{S_W} \Delta \mu(q) \frac{\partial^2}{\partial n_p \partial n_q} \frac{1}{R} dS \quad (20)$$

where $\mu = \phi + \phi_\infty \equiv \Phi$.

This is an integral equation of the first kind for the unknown dipole strength μ . The panel method derived from equation (20) will be referred to as the dipole method. This can be regarded as the velocity field formulation of the total potential method.

Due to the equivalence between dipoles and the vortices, equation (20) can be written in a different form,

$$4\pi \frac{\partial \phi(p)}{\partial n_p} = \int_{S_B} \vec{n}_p \cdot \vec{\gamma}(q) \times \nabla_p \left(\frac{-1}{R} \right) dS + \int_{S_W} \vec{n}_p \cdot \vec{\gamma}(q) \times \nabla_p \left(\frac{-1}{R} \right) dS \quad (21)$$

where $\vec{\gamma} = \vec{n}_q \times \nabla_{2-q} \Phi$. We will refer to the panel method from this equation as the vorticity method.

If we choose the vorticity strength in equation (17), such that it has a given shape function $g(t)$ along the chordwise panels, and the spanwise circulation $\Gamma(s)$ is yet to be determined, then

$$4\pi \frac{\partial \phi(p)}{\partial n_p} = 2\pi \sigma(p) + \int_{S_B} \sigma(q) \frac{\partial}{\partial n_p} \left(\frac{-1}{R} \right) dS + \int_{S_B} \vec{n}_p \cdot \vec{\gamma} \times \nabla_p \left(\frac{-1}{R} \right) dS + \int_{S_W} \vec{n}_p \cdot \vec{\gamma} \times \nabla_p \left(\frac{-1}{R} \right) dS \quad (22)$$

where $\vec{\gamma} = \Gamma(s)g(t)\vec{t}$, \vec{t} , is the direction of the vorticity, and s and t are the spanwise and chordwise coordinates. Given the normal velocity on S_B from the boundary condition and the vorticity shape function $g(t)$, this is a Fredholm integral equation of the second kind for the unknown source strength σ and the spanwise circulation distribution $\Gamma(s)$. This is the form of the original surface source method by Hess [31]. We will refer to this form as the source based method.

Appendix 2

Implementation of the pressure Kutta condition

As stated in the beginning of the paper, the present panel method employs an explicit pressure Kutta condition. The de-

tailed investigation that led to this decision is described in [17]. In this Appendix we will describe the implementation of the pressure Kutta condition on a duct operating in conjunction with a propeller. The implementation of the Kutta condition in the present propeller panel code is very similar.

Green's formula (11) for the perturbation potential on the duct is discretized as follows:

$$\sum_j D_{ij} \phi_j = \sum_j S_{ij} [\vec{U}_E \cdot \vec{n}_j] + \phi^r + \sum_m W_m \cdot \Delta \phi_m \quad (23)$$

where D_{ij} and S_{ij} are the potentials at the control point i due to unit constant strength dipoles and sources, respectively, placed at panel j , and ϕ^r is the perturbation potential due to the propeller. The quantity $\Delta \phi_m$ represents the jump in the potential at the m^{th} strip on the duct wake, and W_m is the influence of the m^{th} dipole wake strip at the i^{th} control point.

The unknown $\Delta \phi_m$ will be determined by applying the Kutta condition at the duct trailing edge.

The Kutta condition requires that the velocity at the trailing edge of the duct be finite. In the numerical formulation of the problem, we will implement the Kutta condition by requiring that the pressures at the upper and lower control points at the trailing edge be equal. This can be expressed as follows:

$$\Delta p_m = p_m^U - p_m^L = 0 \quad \text{for } m = 1, M_b \quad (24)$$

where M is the total number of circumferential panels on the duct, and M_b is the total number of circumferential panels between two blades.

A direct solution of the resulting system of equations (23) and (24) is difficult due to the nonlinear character of equation (24). Therefore an iterative solution algorithm is employed. At the k^{th} iteration, we solve the linear system of equations (23) with the values of $\Delta \phi_m^{(k)}$ determined from the $(k-1)^{\text{th}}$ iteration. The values of $\Delta p_m^{(k)}$ are given by (24), with the values of the pressures p_m^U and p_m^L determined as described in Appendix 3. If $\Delta p_m^{(k)}$ is not equal to zero within the desired tolerance, we proceed to another iteration with $\Delta \phi_m^{(k+1)}$ determined as follows:

$$[\Delta \phi]^{(k+1)} = [\Delta \phi]^{(k)} - [J]^{-1} \cdot [\Delta p]^{(k)} \quad (25)$$

where

$$[\Delta p] = [\Delta p_1, \Delta p_2, \dots, \Delta p_{M_b}]^T \quad (26)$$

$$[\Delta \phi] = [\Delta \phi_1, \Delta \phi_2, \dots, \Delta \phi_{M_b}]^T \quad (27)$$

and $[J]^{-1}$ is the inverse of the Jacobian matrix, the elements of which are defined as

$$J_{ij} = \frac{\partial(\Delta p_i)}{\partial(\Delta \phi_j)} \quad (28)$$

with the values of the partial derivatives approximated numerically as

$$\frac{\partial(\Delta p_i)}{\partial(\Delta \phi_j)} \approx \frac{\Delta p_i^{(l)} - \Delta p_i^{(0)}}{\Delta \phi_j^{(l)} - \Delta \phi_j^{(0)}} \quad (29)$$

where $\Delta p_i^{(0)}$ corresponds to the initial guess $\Delta \phi_j^{(0)}$, and $\Delta p_i^{(l)}$ corresponds to $\Delta \phi_j^{(l)}$, a perturbation to the initial guess defined as

$$\Delta \phi_j^{(l)} = (1 - \beta) \Delta \phi_j^{(0)} \quad (30)$$

and

$$\Delta \phi_l^{(l)} = \Delta \phi_l^{(0)} \quad \text{for } l \neq j \quad (31)$$

where β is a small number. We have selected $\beta = 0.01$, although the algorithm has been found to converge for a large range of β .

The initial guess, $\Delta \phi_m^{(0)}$, is taken as the difference of the potentials at the upper and lower control points at the trailing edge of the duct

$$\Delta \phi_m^{(0)} = \phi_m^U - \phi_m^L \quad (32)$$

The initial guess is therefore the original Morino [16] Kutta condition.

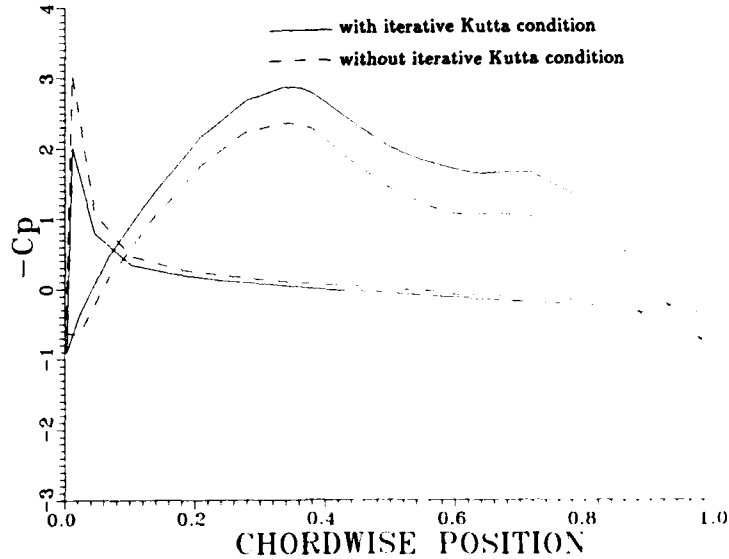


Fig. 29 Comparison of duct chordwise pressure distributions obtained before and after the application of the iterative pressure Kutta condition

Figure 29 shows a typical chordwise pressure distribution on a duct before and after the application of the iterative Kutta condition. The chordwise panel shown in this example is adjacent to the blade tip, where crossflow effects are greatest. It is evident that the pressures at the trailing edge are initially unequal, but become equal after application of the iterative Kutta condition.

Appendix 3

Computation of pressure distributions

After the discrete values of the potential on the body have been computed the pressure distribution on the surface can be determined by applying Bernoulli's equation. We assume that the body rotates with a constant angular velocity Ω since this has a direct application to the propeller or to the duct problem. Calling p the pressure, q , the total fluid velocity with respect to the rotating system, ρ the fluid density, and \vec{r} the vector distance from the axis of rotation, we define the total pressure head, H , according to Batchelor [36] as follows

$$H = \frac{p}{\rho} + \frac{1}{2} q^2 - \frac{1}{2} (\vec{\Omega} \times \vec{r})^2 \quad (33)$$

The flow field around a ducted propeller in axisymmetric flow will be steady when referred to a coordinate system rotating with the propeller. In that case Bernoulli's equation, as shown in Batchelor [36], can be expressed as

$$\nabla H = \vec{q}_t \times (\vec{\omega} + 2\vec{\Omega}) \quad (34)$$

where $\vec{\omega}$ is the vorticity of the fluid with respect to the rotating system. The term $\vec{\omega} + 2\vec{\Omega}$ represents the vorticity vector with respect to the absolute system. Equation (34) requires that the total pressure head along stream surfaces, H_s , remain constant:

$$H_s = \text{constant} = \frac{p_s}{\rho} + \frac{1}{2} U_s^2 \quad (35)$$

where U_s is the axial inflow velocity and p_s the pressure far upstream on the same stream surface.

In the case of uniform inflow, H will be constant everywhere in the flow field.

The total velocity vector \vec{q}_t can be decomposed as follows:

$$\vec{q}_t = \vec{U}_k + \nabla \phi \quad (36)$$

where \vec{U}_k is the relative effective incoming velocity and $\nabla \phi$ is the perturbation velocity at the point under consideration.

To determine the pressure distribution on the body, it is necessary to determine \vec{q}_t at the control points on its surface. If \vec{n} is the normal unit vector on the surface of the body, then according to the kinematic boundary condition on the body

$$\vec{q}_t \cdot \vec{n} = 0 \quad (37)$$

By combining equations (36) and (37), we obtain the result

$$\vec{q}_t = \vec{U}_k - (\vec{n} \cdot \vec{U}_k) \vec{n} + \nabla_s \phi \quad (38)$$

where

$$\nabla_s \phi = \nabla \phi - (\vec{n} \cdot \nabla \phi) \vec{n} \quad (39)$$

The term $\nabla_s \phi$ corresponds to the component of the perturbation velocity tangent to body surface. If we call \vec{s} and \vec{t} the unit vectors tangent to the surface along the two grid directions, the following equations hold:

$$\frac{\partial \phi}{\partial s} = \vec{s} \cdot \nabla_s \phi \quad (40)$$

$$\frac{\partial \phi}{\partial t} = \vec{t} \cdot \nabla_s \phi \quad (41)$$

By using equations (40) and (41) we can express $\nabla_s \phi$ as:

$$\nabla_s \phi = \frac{\frac{\partial \phi}{\partial s} [\vec{s} - (\vec{s} \cdot \vec{t}) \vec{t}] + \frac{\partial \phi}{\partial t} [\vec{t} - (\vec{s} \cdot \vec{t}) \vec{s}]}{\|\vec{s} \times \vec{t}\|^2} \quad (42)$$

The quantities $\partial \phi / \partial s$ and $\partial \phi / \partial t$ correspond to the projections of the perturbation velocity along the two grid directions, and these will be obtained numerically.

In the special case of a duct, $\partial \phi / \partial s$ is determined from the second-order finite difference of the computed values of the potentials at the control points along each chordwise duct station. $\partial \phi / \partial t$ is determined from the derivative of the cubic spline passing through the potentials along each circumferential duct station.

The values of the pressures are computed by using equations (35), (38) and (39). The pressures are finally expressed in terms of the pressure coefficient C_p , which is defined as:

$$C_p = \frac{p - p_s}{\frac{\rho}{2} U_s^2} \quad (43)$$

Appendix 4

Modeling of the tip gap

The radial clearance between the propeller and the interior surface of the duct is generally small compared with the overall dimensions of the device. As a result, a large mismatch in length scale exists between the overall flow around the duct, hub, and propeller blades and the local flow through the tip gap. This would not be a serious problem except for the fact that the local gap flow has a major influence on the global flow. A similar problem is encountered in the analysis of axial flow turbomachines.

The flow around an isolated duct, hub or set of propeller blades can be represented with reasonable accuracy as a potential flow. What really happens when the tip of a propeller blade is brought in close proximity to the duct is not obvious. The characteristics of a potential flow analysis can be seen most easily by examining the solution for a simple lifting line of span s and constant unit downwash $w^* = 1$ operating at a spanwise distance h from an infinite plane wall. The wall can, of course, be represented by an image lifting line. The spanwise distribution of circulation

$$G(y) = \frac{\Gamma(y)}{w^*s}$$

and the distribution of velocity on the wall and in the gap region can be computed using a vortex lattice. The number of vortex lattice panels required for accurate results increases as the gap ratio h/s decreases, but it is easy to obtain *graphically exact* results with very little computing effort.

Figure 30 shows the spanwise distribution of circulation obtained for various gap ratios. The lowest curve is for a relatively large gap ratio of 0.04, while the next four curves show how the circulation changes as the gap is successively halved. Finally, the top curve represents zero gap, where the effect of the wall image is to create the same flow as for an elliptically loaded lifting line of span $2s$. Presenting the results in this way emphasizes the fact that a lifting line with an extremely small gap does not behave at all like one with zero gap, and that an infinitesimal change in the gap produces a large global change in the circulation distribution.

The reason for this can be found in Fig. 31, which shows the distribution of velocity along the wall induced by the lifting line and its image. Here we see that the lifting line with a gap ratio

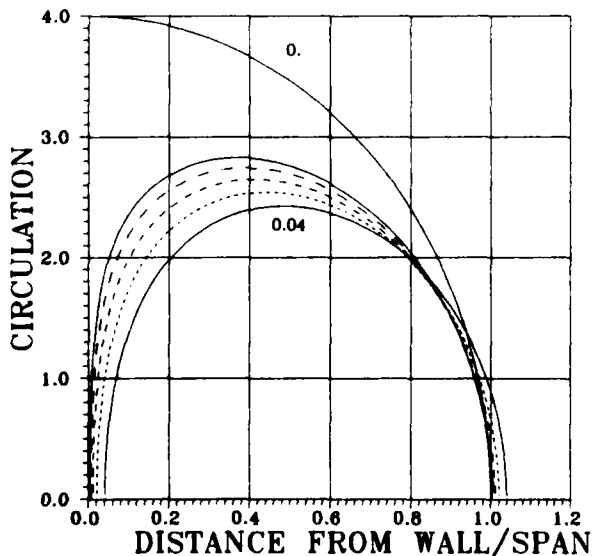


Fig. 30 Nondimensional spanwise circulation distributions, Γ/w^*s , for a lifting line next to a wall for gap ratios $h/s = 0, 0.0025, 0.005, 0.01, 0.02, 0.04$

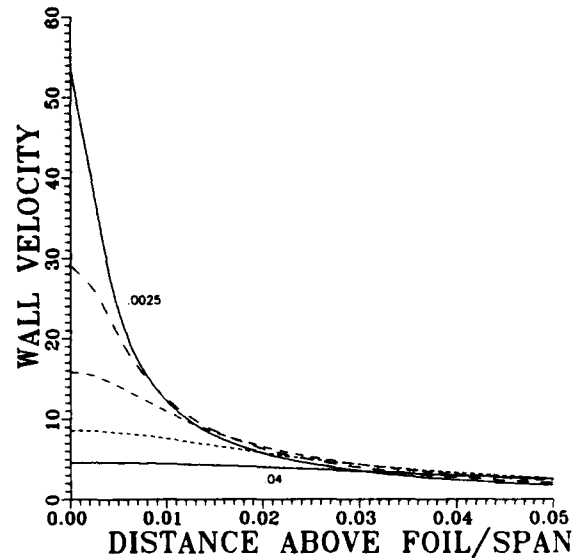


Fig. 31 Nondimensional velocity w/w^* along the wall induced by a lifting line and its image for the same gap ratios

of 0.0025 induces a peak velocity of over 50 times the downwash velocity! While the gap is negligibly small, the existence of such hurricane force flow speeds explains why the circulation is affected everywhere.

Figure 32 shows the volumetric flow through the gap as a function of gap ratio. While the gap flow eventually goes to zero as the gap is closed, it is approximately constant in the range of practical gap ratios, thus indicating that the gap velocities will be roughly inversely proportional to the gap ratio.

These results, however, are contrary to experimental evidence, where it has been found that the circulation distribution tends towards the zero gap limit much more rapidly. A physical explanation is that the cross flow around the tip separates, thus forming

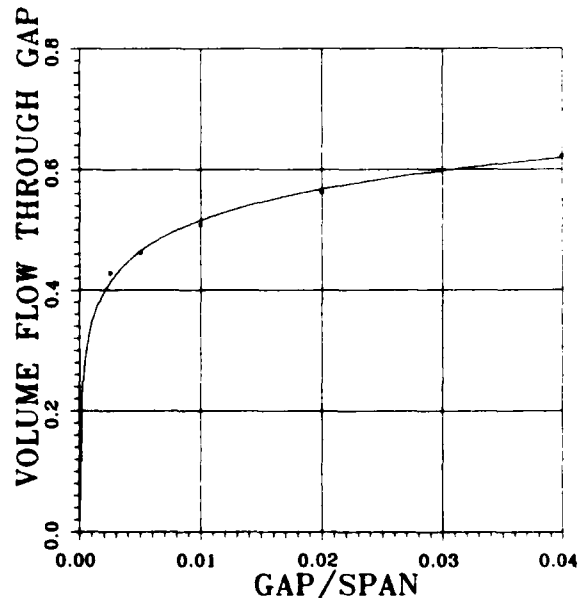


Fig. 32 Nondimensional volumetric flow/unit chord Q/w^*s through the gap between a lifting line and its image as a function of the gap ratio h/s

a *leakage vortex sheet* shown schematically in Fig. 33, taken from Lakshminarayana [6]. This is fundamentally similar to the mechanism of tip vortex generation for a wing or hydrofoil in an unbounded fluid. However, in this case the cross flow is greatly increased due to the presence of the wall, and the flow is further complicated by the presence of the wall boundary layer.

A simple model of the crossflow through the gap which appears in several sources in the turbomachinery literature has been recently reviewed by Van Houten [4]. In this model, the leakage vortex sheets leaving the tip of the physical blade and its image appear as the boundaries of a two dimensional jet when viewed in a plane normal to the blade surface. Thus the flow is approximated by one through an orifice. The relationship between the volumetric crossflow, Q , and the pressure difference driving the flow is

$$Q = hC_o \sqrt{\frac{2\Delta p}{\rho}} \quad (44)$$

where C_o is a discharge coefficient which depends principally on the tip cross-sectional shape, the wall motion, and wall boundary layer characteristics. Typical values compiled by Van Houten [4] range from 0.76 to 0.92.

The recent development of efficient finite-difference methods for solving the two-dimensional Navier-Stokes equations have made it possible to obtain theoretical crossflow solutions for different tip geometries [7]. Such calculations provide a rational basis for determining C_o , but do not alter the fundamental nature of the basic orifice equation.

One can make an order-of-magnitude comparison of the volumetric flow given by equation (44) and the lifting line results plotted in Fig. 32 by equating the pressure difference Δp in equation (44) to the lift on the lift per unit area on the hydrofoil represented by a lifting line. This requires the introduction of an aspect ratio A and a ratio of downwash velocity to inflow speed,

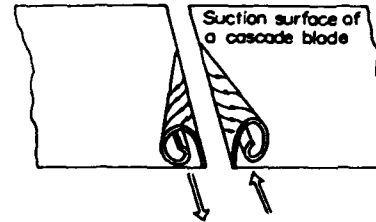


Fig. 33 Schematic of gap vortex formation around a blade tip and its image, from Lakshminarayana [6]

w^*/U . The orifice equation then becomes

$$Q \approx C_o \frac{h}{s} \sqrt{\frac{2C}{(w^*/U) A}} \quad (45)$$

By substituting any reasonable values for the circulation and aspect ratio in equation (45), one concludes that for small gaps, the mass flow driven by the pressure difference across the gap is orders of magnitude smaller than the potential flow value derived from lifting line theory. On the other hand, for large gaps, where the idealization of two-dimensional orifice flow becomes less valid, the flow predicted from (45) is of the same order of magnitude as the lifting line value.

While the ducted propeller flow problem is more complicated, the trend must be similar. A potential flow representation of the blades and duct is suitable for either large clearances or zero clearance, where there is no flow around the tip. However, for small clearances one must either turn to a complete three-dimensional viscous flow solution in the tip gap region, or adopt some means of coupling the potential flow solution to a local representation of the viscous crossflow in the gap.